



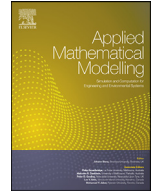
An improved air entrainment model for stepped spillways

Downloaded from: <https://research.chalmers.se>, 2024-04-26 15:43 UTC

Citation for the original published paper (version of record):

Almeland, S., Mukha, T., Bensow, R. (2021). An improved air entrainment model for stepped spillways. *Applied Mathematical Modelling*, 100: 170-191.
<http://dx.doi.org/10.1016/j.apm.2021.07.016>

N.B. When citing this work, cite the original published paper.



An improved air entrainment model for stepped spillways

Silje Kreken Almeland^{a,*}, Timofey Mukha^b, Rickard E. Bensow^b

^a Norwegian University of Science and Technology, Department of Civil and Environmental Engineering, Trondheim NO-7491, Norway

^b Chalmers University of Technology, Department of Mechanics and Maritime Sciences, Hörsalsvägen 7A, Gothenburg SE-412 96, Sweden

ARTICLE INFO

Article history:

Received 9 September 2020

Revised 7 July 2021

Accepted 18 July 2021

Available online 14 August 2021

Keywords:

Air entrainment modelling

Numerical modelling

CFD

Openfoam

Self-aeration

Stepped spillway

ABSTRACT

This work considers the application of the air entrainment model developed in [P. Lopes et al. *Int. J. Nonlin. Sci. Num.*, vol. 18, pp. 559–574, 2017] to simulation of flows in stepped spillways. Four Froude numbers are considered for the flow, with parameters selected to match available experimental data. An extensive simulation campaign led to the identification of several deficiencies in the model, most importantly, its strong grid dependence. An improvement to the interface detection algorithm used in the model is proposed, and simulations reveal improved robustness with respect to the grid density. Furthermore, two criteria for predicting the inception point of air entrainment are tested, based on energy balance and boundary layer state, respectively. The boundary layer-based approach is recommended due to superior accuracy and robustness with respect to turbulence model selection.

© 2021 The Author(s). Published by Elsevier Inc.
This is an open access article under the CC BY license
(<http://creativecommons.org/licenses/by/4.0/>)

1. Introduction

Along with a renewed interest in stepped spillways as a flood overflow structure and energy dissipator in hydraulic engineering, attempts at gaining a better physical description of stepped spillway flows have also intensified. A process that is especially challenging to study by means of both physical experiments and numerical simulations, is the self-aeration of the spillway. Yet, since large quantities of entrained air lead to higher flow depths, release energy, and reduce the potential for damage caused by cavitation, accurate prediction of aeration is crucial for spillway design. In this work, mathematical modelling and simulation of air entrainment is in focus. To put the present contribution into context, a brief review of the physics of air entrainment in stepped spillways is given below, followed by an overview of past attempts of accounting for them in a numerical setting.

Generally, air entrainment is driven by turbulent motion and occurs when the turbulent forces at the free surface overcome the stabilizing effects of surface tension and buoyancy [1]. Applied to spillways, it has been widely accepted since the early work of Straub and Anderson [2] that the onset of self-aeration takes place when the turbulent boundary layer, developed from the crest, reaches the free surface. This location is commonly referred to as the ‘inception point’. Several contributions consider the onset of the aeration in detail [3–7], and empirical relations exist for the distance to the inception point from the spillway crest [8–10]. We recommend [5] for an overview of these efforts. Boes and Hager [8] proposed a computable definition of the inception point as the location where the pseudo-bottom air concentration is 0.01. The pseudo-

* Corresponding author.

E-mail addresses: silje.k.almeland@ntnu.no (S.K. Almeland), timofey@chalmers.se (T. Mukha), rickard.bensow@chalmers.se (R.E. Bensow).

bottom refers to the line created by the tangent line between subsequent step edges and does not represent the actual step surfaces.

Downstream of the inception point, entrainment quickly leads to a complete distortion of the perceivable air–water interface into a thick layer occupied by a mixture of the two phases. Furthermore, experimental data exhibits a non-negligible concentration of air all the way down to the surface of the steps. The work of Pfister and Hager [11] presents a detailed account of the transport mechanism responsible for that. It is shown that transiently occurring air troughs can penetrate deep enough to hit the edge of the steps. This leads to break-up and eventual entrapment of air pockets in the recirculating flow occupying the corners of the steps.

An important property of stepped spillway flow is that it eventually reaches a state where its average properties no longer alter in the streamwise direction. The associated distributions of flow variables are referred to as uniform conditions. The part of the flow preceding this state is called the development region. Empirical expressions for the extent of the development region have been given by several authors [10,12], as well as relations for the surface height in the different flow regions along the spillway [8–10].

When it comes to numerical modelling of the complicated multiphase physics discussed above, one can generally distinguish two approaches. One is to try to explicitly capture these phenomena using a high-fidelity scale-resolving simulation framework. (Large-eddy simulation, preferably coupled with a geometric interface capturing method, e.g. [13]). This necessitates using very dense computational grids and therefore consuming vast amounts of computational resources. For this reason, results from such simulations of spillways have not yet been reported in the literature. However, works on other aerating flows can be found, e.g. [14] for the case of the hydraulic jump.

The alternative approach is to introduce an additional model accounting for the entrainment of air. Different ways of introducing such modelling have been proposed, also varying in the general multiphase simulation methodology into which they are fit. Normally, interface capturing methods are used for stratified flows, where the important length scales are several times the cell size of the computational mesh. For dispersed two-phase flows, where a substantial part of the two-phase structures are smaller than the computational grid, a two-fluid (Euler–Euler) framework is generally used. However, in the case of aerated flows, there are typically some flow regions belonging to the stratified regime, and others with active mixing. This makes using both interface-capturing and Euler–Euler approaches equally challenging, with advantages and disadvantages in both.

Efforts within the framework of the two-fluid model have been reported in [15–19]. The main benefit of having a separate set of equations for each phase is the possibility to introduce interaction terms between the entrained air bubbles and the surrounding fluid. Naturally, the extra equation set also leads to increased computational costs. In the context of interface capturing methods, such as Volume of Fluid (VoF), the general idea is to introduce air entrainment as a subgrid model. In regions where the model is inactive, accurate resolution of the interface remains possible. Here the study of Hirt [20] can be distinguished as pioneering. This model was implemented in FLOW-3D® and has been used in publications on stepped spillways [21–24]. Lopes et al. [25] incorporated the entrained air flux estimator developed in [18] into a VoF framework by introducing a separate transport equation for the entrained air. The solver is implemented in OpenFOAM®, and results from stepped spillway simulations are presented in the article.

In this work, we present further developments of the model by Lopes et al. [25]. To motivate the need for improvements, results from a simulation campaign, in which the model in its current formulation is applied to stepped spillway flow at four different Froude numbers, are presented. The simulations constituting the campaign vary in the employed grid resolutions and parameters of the model. Modifications to the transport equation for entrained air are proposed, as well as an alternative inception point detection algorithms. Results from a second simulation campaign, in which the modified model is tested, are then presented. Better performance in terms of accuracy and robustness is revealed, making the improved model a suitable candidate for computationally efficient low-fidelity simulations of stepped spillway flow. The article is supplemented by a dataset containing all the simulation results.¹

The remainder of this article is structured as follows. Section 2 describes the computational methods used in the performed computations. In Section 3, the setup of the stepped spillway simulations is discussed. Section 4 presents the air entrainment model developed by Lopes et al. [25]. Section 5 contains results from the simulation campaign in which the model of Lopes et al. [25] is used. An analysis of the mean velocity profiles in the spillways is given in Section 6. Improvements to the air entrainment model are then proposed in Section 7, and corresponding simulation results are provided in Section 8. Concluding remarks are given in Section 9.

2. Computational fluid dynamics methods

2.1. Governing equations

The flow was simulated using the Volume of Fluid (VoF) multiphase modelling technique [26], in which a single set of governing equations is solved for all phases and the location of the interface is identified based on the values of the cell volume fraction of the liquid phase, α_l . Both fluids are considered incompressible and immiscible. Furthermore, Reynolds

¹ 10.6084/m9.figshare.12782339

averaged Navier-Stokes (RANS) turbulence modelling is adopted, leading to the following set of governing equations [27].

$$\frac{\partial \rho \bar{\mathbf{u}}}{\partial t} + \nabla \cdot (\rho \bar{\mathbf{u}} \otimes \bar{\mathbf{u}}) = -\nabla \bar{p}_{\rho gh} - \mathbf{g} \cdot \mathbf{x} \nabla \rho + \nabla (\mu (\nabla \bar{\mathbf{u}} + (\nabla \bar{\mathbf{u}})^T) - \rho \overline{\mathbf{u}' \otimes \mathbf{u}'} + \mathbf{f}_s \quad (1)$$

$$\nabla \cdot \bar{\mathbf{u}} = 0. \quad (2)$$

Here the overbar denotes the Reynolds average, ρ is the density, μ is the dynamic viscosity, $\bar{\mathbf{u}}$ is the time averaged velocity vector, $p_{\rho gh} = p - \rho \mathbf{g} \cdot \mathbf{x}$ is the dynamic pressure, and \mathbf{f}_s is the surface tension force. The latter is approximated using the Continuous Force Model, see [28] and also [29] for a detailed discussion in the context of OpenFOAM®. The term $\rho \overline{\mathbf{u}' \otimes \mathbf{u}'}$ represents the Reynolds stresses, which are to be approximated by the turbulence model.

An algebraic approach to account for the evolution of α_l is adopted, with the associated transport equation originally formulated as

$$\frac{\partial \alpha_l}{\partial t} + \nabla \cdot (\bar{\mathbf{u}} \alpha_l) + \nabla \cdot (\mathbf{u}^c (1 - \alpha_l) \alpha_l) = 0, \quad (3)$$

in OpenFOAM®'s VoF solvers. The third term in the equation is artificial and is meant to introduce additional compression of the interface to ensure its sharpness. However, here the formulation of this term is modified in order to accommodate it into the air entrainment modelling framework. The details are provided in Section 4. The definition of \mathbf{u}^c is nevertheless not altered: It is aligned with the interface normal, and its magnitude is computed as $C_\alpha |\bar{\mathbf{u}}|$, where C_α is an adjustable constant, here set to 1.

Given α , the material properties of the fluids are readily obtained as

$$\rho = \alpha_l \rho_l + (1 - \alpha_l) \rho_{air}, \quad \mu = \alpha_l \mu_l + (1 - \alpha_l) \mu_{air}. \quad (4)$$

The indices l and air are used to refer to the water and air, respectively.

What remains to be discussed is the choice of turbulence model, which for the case of the stepped spillway is far from trivial. In principle, the model should be able to properly account for the interaction between the turbulent and multiphase structures in order to provide accurate prediction in the aerated region of the flow. None of the closures that have found widespread use were developed with this goal in mind. Nevertheless, it is common for conventional two-equation models to be used for aerated flows. In [25], which is the work this article largely builds upon, the $k - \omega$ SST model [30] is used for stepped spillway simulations. In [18], it is employed in simulations of a plunging jet and a hydraulic jump. For the latter, many studies also use the $k - \epsilon$ model and its variations, a comprehensive list of references can be found in Table 5 in [31]. Qian et al. [32] found the realisable $k - \epsilon$ model to be favourable for stepped spillway flow. Based on the above, we consider both the $k - \omega$ SST and the realisable $k - \epsilon$ model [33] and test which of them leads to better predictive accuracy.

It is pointed out in [34] that in the implementation of the above (and also other) turbulence models in OpenFOAM® the viscous diffusion terms are not treated consistently in regions with a non-zero density gradient. Since in the simulations of the spillway presented here a density gradient is present across the whole aerated part of the flow, this issue can have a significant effect on the results. The authors of [34] also provide alternative implementations, in which the inconsistency is resolved. Here, we test using both the default and the improved implementations.

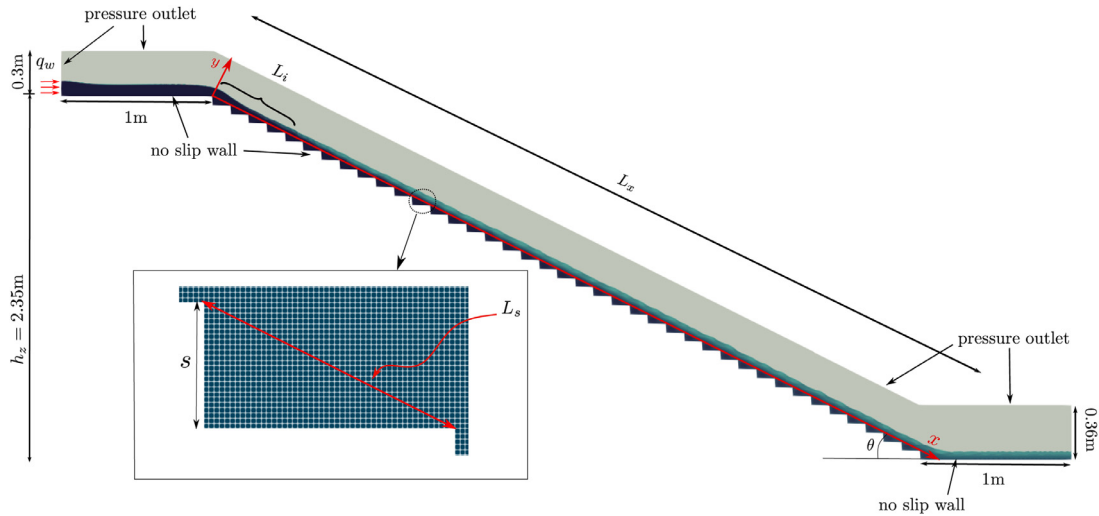
2.2. Numerical methods

The computations are performed using OpenFOAM® version 5, provided by the OpenFOAM Foundation. This Computational Fluid Dynamics (CFD) tool is based on cell-centered finite volume discretization, which is de facto the industry standard. Two custom solvers are used in the study, implementing the air entrainment modelling presented in Sections 4 and 7. Both of them represent modifications of the solver `interFoam`, which is distributed with OpenFOAM®. This solver implements the VoF methodology discussed in Section 2.1. The governing equations are solved in segregated manner using a variant of the PISO algorithm [35].

A crucial component of the numerical setup is the selection of the spatial interpolation and time integration schemes. Generally, linear interpolation can be used in space except when considering convective fluxes. In the momentum equation, the latter are interpolated using the `limitedLinearV` scheme, which is a total variation diminishing (TVD) scheme based on the Sweby limiter [36]. The limiter is computed based on the direction of most rapidly changing gradient and then applied to all three velocity components. This improves stability but at a certain expense in terms of accuracy. For the convection of α in equation (3), a TVD scheme using the SuperBee limiter is used. The van Leer limiter was also considered, but SuperBee led to better results on coarser meshes due to being more compressive. Unfortunately, in a multi-dimensional setting, using a TVD scheme does not guarantee that the values of α will be bounded between 0 and 1. Therefore, OpenFOAM® utilizes an additional flux limiting technique, referred to as MULES (Multidimensional Universal Limiter for Explicit Solution). It is based on the Flux Corrected Transport theory developed Zalasak [37], more details can be found in [38]. The convective fluxes in the turbulence equations are discretized using the second order upwind scheme, called `linearUpwind`. This scheme is unbounded, but no significant effect of parasitic oscillations was observed even on coarse grids. Finally, as discussed in Section 4.2 below, the air entrainment model adds an advection-diffusion equation for the flow variable α_g , meant

Table 1Setup for the different simulation cases. The number of cells are given in 10^3 .

$F_s(-)$	$\theta(^{\circ})$	$s(\text{m})$	$q(\text{m}^2\text{s}^{-1})$	$L_x(\text{m})$	$L_y(\text{m})$	$h_{\text{win}}(\text{m})$	$n_{\text{cells},G1}$	$n_{\text{cells},G2}$	$n_{\text{cells},G3}$	$n_{\text{cells},G4}$
2.7	26.6	0.06	0.07	5.23	0.134	0.10	89	354	1 414	5 647
4.6	18.4	0.06	0.11	7.41	0.190	0.13	122	482	1 917	7 646
8.3	18.4	0.03	0.07	7.41	0.095	0.10	119	466	1 840	7 317
13.0	18.4	0.03	0.11	7.41	0.095	0.13	119	466	1 840	7 317

**Fig. 1.** Sketch of the geometry of the simulation case, identifying the geometric parameters, and also the employed boundary conditions.

to indicate the distribution of the volume fraction of entrained air, to the system. Here, a TVD scheme using the van Leer limiter is employed.

The first-order implicit Euler scheme was used for time-stepping. The choice is not of particular importance here because the flow eventually arrives to an essentially steady state. Nevertheless, a Courant-Friedrichs-Lewy (CFL) number ≤ 1 was necessary to maintain in order to keep the simulations stable. This was achieved using adaptive time-stepping.

3. Simulation cases

This section presents the setup of the stepped spillway simulations used to evaluate the performance of the entrainment modelling. In order to have a reference with respect to which the accuracy of simulation results can be analysed, the flow and spillway parameters are selected to match those in the experiments of Bung [10]. These were performed on four different stepped spillways combining two selections for the angle ($\theta = 18.4, 26.6^{\circ}$) with two for the step height ($s = 0.03, 0.06$ m). For each spillway, measurements were made for three flow discharge values ($q = 0.07, 0.09, 0.11 \text{ m}^2\text{s}^{-1}$). The parameters θ , s , and q can be used to construct the step Froude number, which can be considered the main controlling parameter of the flow [9,39],

$$F^s = \frac{q}{\sqrt{g \sin \theta K^3}}. \quad (5)$$

Here $K = s \cos \theta$ is the step induced macro-roughness and g is the acceleration due to gravity. The experiments of Bung cover twelve different Froude numbers in the range, $2.7 \leq F^s \leq 13$. For the simulations four values fairly evenly distributed across this range have been selected: 2.7, 4.6, 8.3, and 13.0. The values of θ , s , and q in the four simulation cases are provided in Table 1. This table also provides the values of some auxiliary geometrical parameters, the definition of which can be found in Fig. 1. The figure also shows the origin and orientation of the employed Cartesian coordinate system.

All the simulations are performed on 2D domains. This is chiefly motivated by the fact that the investigated modelling methodology is low-fidelity and most suitable for quick evaluations of the integral characteristics of the flow. Any 3D effects due to sidewalls are expected to be negligible with respect to the overall accuracy of the flow predictions. Additionally, using 2D domains seems to ensure that, even on dense grids, no air entrainment is resolved by the VoF. This is shown by the *interFoam* computations on grid G4. By contrast, in a 3D setting, it is more likely that some interface perturbations eventually start getting captured. Investigating the performance of the entrainment modelling in such a scenario is of interest, but lies out of scope of the current work.

Table 2
Simulation parameters.

Property	Value
Liquid density, ρ_l	1000 kg/m ³
Gas density, ρ_{air}	1 kg/m ³
Liquid kinematic viscosity, ν_l	$1 \cdot 10^{-6}$ m ² /s
Gas kinematic viscosity, ν_{air}	$1.48 \cdot 10^{-5}$ m ² /s
Surface tension coefficient, σ	0.07

The same boundary conditions were used for all cases, with the exception of the discharge q prescribed at the water inlet. The height of the inlet was adjusted to ensure sub-critical inflow conditions. A zero gradient condition was used for the pressure, while Dirichlet conditions were applied to k , ϵ , and ω . The values were set assuming 5% turbulent intensity and 10% of the critical height as the turbulent length scale.

For the outlet, a zero gradient condition was prescribed for velocity, pressure, α_l and α_g . Here α_g is the modelled volume fraction of air, introduced within the air entrainment model described in Section 4. For k , ϵ , and ω the OpenFOAM `inletOutlet` boundary condition was applied. It acts as a zero gradient condition in case of outflow, but for backflow a homogeneous Dirichlet condition is applied instead.

No-slip conditions were used at the walls, with a zero gradient condition set for α_l and α_g . The turbulent quantities were estimated by regular wall laws, in OpenFOAM named as `kqRWallFunction`, `epsilonWallFunction`, `omegaWallFunction` and `nutkWallFunction`, for k , ϵ , ω , and ν_t respectively.

For the top boundary the total pressure was fixed, and a `pressureInletOutletVelocity` condition was applied for the velocity. Similar to `inletOutlet`, this imposes a zero gradient for outflow, whereas for backflow, it assigns a velocity based on the flux in the patch normal direction. The `inletOutlet` boundary condition was used for α_l , α_g , k , ϵ , and ω .

The material properties of the fluids were set to correspond to air and water. The values are provided in Table 2.

The computational grids were constructed using Pointwise®, and consist of square cells with the exception of a small strip close the top boundary, where unstructured meshing was necessary to account for the slope of the geometry. Four grids with increasing cell density, denoted G1, G2, G3, and G4, were constructed for each of the four spillways. In each consecutive grid the edge length of the square cells is halved. On the coarsest grid G1, the edge length is 5 mm, which corresponds to what was used in the simulations by Lopes et al. [25]. This can be related to the critical height of the spillway flow, defined as $h_c = (q^2/g)^{1/3}$. Depending on the flow case, on the G1 grid, h_c is discretised by either 15 or 21 cells. The numbers for the G4 grid are, respectively, 126 and 171. The densities are not adjusted to remain equal with respect to h_c across all flow conditions, because experiments showed that the relevant parameter for entrainment modelling is the resolution of the interface. The number of cells in each mesh is given in Table 1.

In conclusion, additional characteristic scales of stepped spillway flow are defined. These will be used for non-dimensionalising the results. At a given x , the height h_{90} is defined as the y -coordinate of the point where $\alpha_{air} = 0.9$. The velocity u_{90} is defined as the x -component of the mean velocity vector at $y = h_{90}$. Similar scales can be defined with respect to other α_{air} values, e.g. h_{50} .

4. Air entrainment modelling

This section presents the air entrainment model developed by Lopes et al. [25]. One can split the model into three components: an estimator for the flux of entrained air, a transport equation for the volume fraction of entrained air, and a coupling procedure between the model and the VoF framework. Sections 4.1, 4.2, and 4.3 each focus on one of these components. Additionally, for the stepped spillway, estimating the location of the inception point is necessary and this constitutes an additional component of the model, which is treated in Section 4.4. An overview of the air entrainment model is given in Fig. 9 in Section 7.

4.1. Estimating the flux of entrained air

A key component of the model is the estimation of the quantity of entrained air carried past some imaginary surface located below the interface. The estimate was proposed by Ma et al. [18]:

$$\mathbf{q} = a \cdot \text{Pos}(\nabla(\mathbf{u} \cdot \mathbf{n}) \cdot \mathbf{n}), \quad (6)$$

where a is a length scale associated with the roughness of the interface due to turbulence,

$$\text{Pos}(x) = \begin{cases} x, & x \geq 0 \\ 0, & x < 0, \end{cases}$$

and \mathbf{n} is the interface normal defined as

$$\mathbf{n} = \nabla\alpha_l / (|\nabla\alpha_l| + \varepsilon). \quad (7)$$

Here ε is a small number added for numerical stability.

It is assumed that entrainment is confined to a layer of thickness ϕ_{ent} close to the surface. Therefore, in order to obtain a volumetric air entrainment rate, \mathbf{q} can be divided by ϕ_{ent} . Note, however, that (6) is by definition not restricted to being non-zero only in the vicinity of the interface. Theoretically, entrainment can be incorrectly predicted in regions where it should not take place. For this reason, in [25], \mathbf{q} is additionally multiplied by some function δ_{fs} , which is non-zero only close to the interface. The final form of the volumetric air entrainment rate estimate is

$$S_g = \frac{a}{\phi_{ent}} \text{Pos}(\nabla(\mathbf{u} \cdot \mathbf{n}) \cdot \mathbf{n}) \delta_{fs}. \quad (8)$$

It remains to define how a , ϕ_{ent} , and δ_{fs} are computed. The common approach for a is to equate it to the turbulent length scale as predicted by the RANS model. The value of ϕ_{ent} should be related to some characteristic length scale of the problem.

Within the VoF framework, the α_l -field stands out as the natural choice as a basis for the development of an interface indicator function such as δ_{fs} . Typically, the interface is defined as the isosurface $\alpha_l = 0.5$, however this is only accurate when the interface is sharp. In the presence of air entrainment, a more robust metric is the magnitude of the gradient of α , which can be expected to reach its maximum close to the boundary between the continuous air region and the air-water mixture. Hansch et al. [15] used the gradient of α and a function based on tanh to find the interface as part of their air entrainment model. This function was adopted by Lopes et al. [25] and reads as

$$\delta_{fs} = \frac{1}{2} \tanh[\beta \Delta x (|\nabla \alpha_l| - |\nabla \alpha_l|_{cr})] + 0.5. \quad (9)$$

Here $|\nabla \alpha_l|_{cr}$ is a constant representing the critical value of the gradient that is expected to be reached in the interface cells. Its estimate can be computed based on the size of the grid cell, Δx : $|\nabla \alpha_l|_{cr} = 1/(4\Delta x)$. The parameter β can be used to control the extent of the interface region with respect to the chosen $|\nabla \alpha_l|_{cr}$, and thus provides an opportunity to broaden or restrict the number of cells in which the source term is active.

4.2. The α_g -equation

The source term (8) is introduced into an additional equation for the modelled volume fraction of entrained air, α_g :

$$\frac{\partial \alpha_g}{\partial t} + \nabla \cdot (\mathbf{u}_g \alpha_g) + \nabla \cdot \left(\frac{\nu_t}{Sc} \nabla \alpha_g \right) = S_g. \quad (10)$$

Here ν_t denotes the turbulent viscosity, and Sc is the Schmidt number, which in the model of Lopes is considered to be equal to 1. The velocity of the entrained air, \mathbf{u}_g , is either set to be equal to $\bar{\mathbf{u}}$ or alternatively modified according to [40]:

$$\mathbf{u}_g = \bar{\mathbf{u}} + \mathbf{u}_r, \quad (11)$$

where the bubble rise velocity \mathbf{u}_r is calculated based on a bubble radius according to

$$\mathbf{u}_r = \begin{cases} -4474 r_b^{1.357} \frac{\mathbf{g}}{|\mathbf{g}|}, & \text{if } 0 < r_b \leq 7 \times 10^{-4} \text{ m} \\ -0.23 \frac{\mathbf{g}}{|\mathbf{g}|}, & \text{if } 7 \times 10^{-4} < r_b \leq 5.1 \times 10^{-3} \text{ m} \\ -4.202 r_b^{0.547} \frac{\mathbf{g}}{|\mathbf{g}|}, & \text{if } r_b > 5.1 \times 10^{-3} \text{ m}. \end{cases} \quad (12)$$

Which method to apply for the calculation of \mathbf{u}_g is left as a user choice. The inclusion of the turbulent diffusion term in (10) is considered optional.

Additionally, Lopes et al. [25] argue that to properly account for the break-up of bubbles at the free surface, air should not be entrained when $\alpha_{air} = 1 - \alpha_l$ exceeds a certain threshold value, indicating that one are basically within the air phase. In the model, this means that the source term, S_g , in the α_g -equation (10) is deactivated in cells exceeding this threshold. This criterion is referred to as the bubble breakup criterion (BBA). The suggested value to use is 0.1. The reasoning behind this argument is not fully understood by us, but different values of BBA are nevertheless tested below.

The exact physical meaning of α_g and its relation to α_l are somewhat elusive. In [25], the authors discuss the possibility of using the entrainment model without backward coupling to the VoF solver. In this case, the situation is clear: α_g shows the modelled distribution of the volume fraction of entrained air, which cannot be captured by the VoF. However, when the coupling is two-way (particulars presented below), the idea is that the entrained air should be captured in the α_l field, and α_g is essentially reduced to a buffer-field used to propagate the effect of S_g onto α_l .

4.3. Coupling to the VoF solver

Lopes et al. propose two alternatives for coupling the subgrid model with the VoF solver. The first option is one-way coupling, meaning that the α_g field is computed based on the $\bar{\mathbf{u}}$ and ν_t fields obtained in the VoF solution, but doesn't affect this solution itself. This approach only allows for a crude evaluation of where air entrainment can be expected to

occur. Here, we are interested in the other alternative, which is two-way coupling, meaning that the model's predictions should be propagated into the distribution of α_l .

The premise is that the VoF simulation by itself does not resolve any entrainment, and therefore all of it is accounted for by a subgrid model based on the α_g equation (10). The overall idea is that non-zero values of α_g should be reflected in the VoF by an increase of α_{air} in the same region.

Here this is done through a modification of the artificial compression term introduced into the α_l -equation (3):

$$\nabla \cdot (\mathbf{u}^c (1 - \alpha_l) \alpha_l). \quad (13)$$

The term $(1 - \alpha_l) \alpha_l = \alpha_{air} \alpha_l$ is originally meant to serve as an indicator for cells constituting the interface, in which the compression is to be applied. The key observation is that multiplying \mathbf{u}^c by some negative number instead would lead to interface expansion and thus a region occupied by a mixture. The goal is then to correlate α_g with the change in sign in the term in front of \mathbf{u}^c . The most obvious way to do that is exchange $\alpha_{air} \alpha_l$ for $(\alpha_{air} - \alpha_g) \alpha_l$. Note that since (13) is a transport term, mass conservation is guaranteed. The modified α_l -equation then reads

$$\frac{\partial \alpha_l}{\partial t} + \nabla \cdot (\bar{\mathbf{u}} \alpha_l) + \nabla \cdot (\mathbf{u}^c (\alpha_{air} - \alpha_g) \alpha_l) = 0. \quad (14)$$

Under the definition above, the model is active only when $\alpha_g > \alpha_{air}$, which is reasonable. It is also worth mentioning that otherwise (13) recovers its original compressive function. This occurs even in the regions occupied by a mixture, which can be called into question. As part of the work on improving the model, some experiments have been conducted in which positive values of $\alpha_{air} - \alpha_g$ were cut to 0, however the exhibited results were inaccurate, and introducing such a discontinuity is probably best avoided.

4.4. Inception point estimation

As discussed in the introduction, surface aeration initiates when the turbulence perturbations exceed the stabilizing forces of surface tension and buoyancy at the free surface. In the model of Lopes et al. [25] no attempt is made to explicitly compute the force balance. Two model parameters, k_c and u_c , are introduced, where k and u denote turbulent kinetic energy and velocity, and the subscript c stands for critical. The inception is considered to occur when

$$k > k_c \text{ and } \mathbf{u} \cdot \mathbf{n} > u_c \text{ and } \mathbf{u} \cdot \frac{\mathbf{g}}{|\mathbf{g}|} > u_c. \quad (15)$$

Appropriate values for k_c and u_c are extremely difficult to predict a priori, since the selection clearly depends not only on the flow conditions (see Section 5.1), but also on the turbulence model and its prediction of k . Careful calibration with respect to the selected model is therefore necessary. In [25], the authors nevertheless suggest $u_c = 0.8$ m/s and $k_c = 0.2$ m²/s², referring to previous experimental results. Unfortunately, how these values relate to the characteristic length and velocity scales of the flow is not discussed. Relevant works in this regard are [7,41], but clear practical guidelines have not yet been established.

5. Stepped spillway simulations with the original model

This section demonstrates results from simulations performed using the model of Lopes et al. [25] described in the previous section. In the original source the model was reported to reproduce experimental data on a stepped spillway with $F_s = 2.7$. However, the simulations were performed on relatively coarse grids, with the grid sensitivity study performed using only the baseline VoF solver, *interFoam*. Furthermore, initial testing within this work indicated that its effect was reduced upon grid refinement, which motivates the analyses herein.

The implementation of the corresponding solver, called *airInterFoam* was kindly provided by P. Lopes via personal communication. Below, we abbreviate *airInterFoam* to AIF. In the following sections, the solver is evaluated in terms of sensitivity to flow conditions (Section 5.1), grid resolution (Section 5.2), and several parameters of the entrainment model (Section 5.3).

5.1. Sensitivity to F_s

Here, results from four AIF simulations varying in the prescribed Froude number of the stepped spillway flow are presented. To highlight the effect of the entrainment model, data obtained with the baseline VoF solver *interFoam* (abbreviated IF henceforth) are also provided. The employed numerical parameters are based on [25], where good results for the $F_s = 2.7$ case (simulated in 3D) are presented. In particular, the G1 grid is employed, $k - \omega$ SST is used for turbulence modelling, the diffusion term is omitted in the α_g equation, and $k_c = 0.2$ m²/s², $u_c = 0$, $u_g = u_l$, $BBA = 0.1$, and $\phi_{ent} = 0.05 h_c$.

Fig. 2 shows the obtained values of α_{air} in the uniform flow region. Good accuracy is achieved for $F_s = 2.7$ and 4.6, but for the two higher F_s the model fails to predict the reduced penetration of air into the corners of the steps. As a result, in terms of magnitude, the errors in the IF and AIF simulations are similar, although in the case of IF the diffusion of the interface is a purely numerical effect. It is also interesting to note that for $F_s = 2.7$ the accuracy is on par with the 3D simulations using similar model settings conducted in [25].

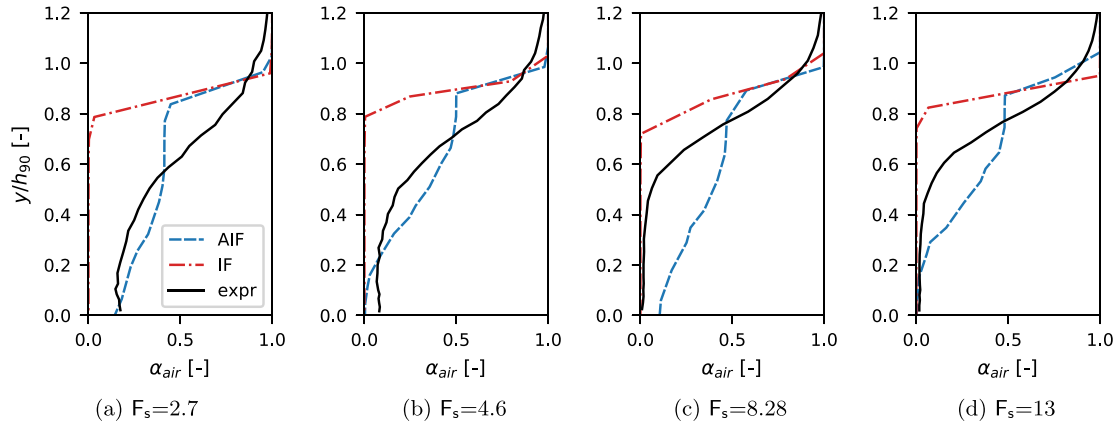


Fig. 2. Vertical void fraction profiles for uniform flow conditions. Stepped spillway flows with different Froude numbers at the coarsest grid G1. AIF simulations compared to IF simulations and experimental results by Bung [10].

The evolution of the surface elevation, measured as h_{90} , is shown in Fig. 3. The elevation's value in uniform conditions is well-predicted for all Froude numbers. However, the location of the inception points are not captured as consistently. The difference in the obtained values with respect to the experimental data of Bung is provided in each plot of the figure: Δn_i stands for the difference in terms the step number, and ΔL_i in terms of x . The obtained inception point locations for $F_s=2.7$ and $F_s=4.6$ are reasonably accurate, but, unfortunately, at higher F_s the disagreement with the experiment becomes larger. Furthermore, the predicted inception point for $F_s=8.3$ is further downstream as compared to that for $F_s=13$, whereas the experimental data exhibits the opposite trend.

Fig. 3 additionally shows the experimental values of h_w , which is the equivalent clear water depth, i.e. the surface elevation that should be predicted by IF. In the obtained results, IF somewhat over-predicts h_w , the reason being the coarseness of the grid.

The predicted profiles of the streamwise velocity are shown in Fig. 4. Remarkably, no effect of air entrainment modelling is visible, and accurate profiles can be predicted with IF. This result was reproduced in all the simulations in this paper, and, for that reason, velocity profiles are not further used to assess model performance. However, it is interesting to compare the form of the profiles with existing empirical estimates, which is done in Section 6.

The principal conclusion from the obtained results is that the settings used in [25] for the $F_s=2.7$ case fail to provide consistently accurate results as the Froude number becomes larger. This indicates that some parameter values of the model, for example k_c , should be made a function of F_s .

5.2. Grid sensitivity

To explore the grid sensitivity of AIF, the $F_s=2.7$ -case was run on all four grids G1-G4. The resulting α_{air} and h_{90} profiles are shown in Fig. 5. Clearly, the behaviour obtained on the coarse grid G1 is substantially changed as the grid gets denser. With increasing resolution, less air is distributed towards the pseudo-bottom, and for the densest grid only a tiny air layer is found close to the surface. The profiles, both h_{90} and α_{air} , approach the corresponding solutions obtained with IF. Obviously, this is caused by the fact that less numerical diffusion contributes to the transport of α_g as the grid is refined, but inspection shows that this is also caused by the shrinkage of the area in which the source term S_g is non-zero. This, in turn, is controlled by δ_{fs} , which makes the definition of this function a contributor to the grid sensitivity. A more elaborate discussion follows in Section 7. On the other hand, with respect to h_w , the IF solution consistently improves with grid refinement. On the G4 grid the interface is perfectly sharp and the h_w profile is very well-matched.

5.3. Sensitivity to u_r , bubble breakup criterion, and α_g -diffusion

Here we explore the effects of some of the components of the entrainment model. First, the impact of the air bubble drift velocity model, as given in eq. (12), is investigated. This is followed by an analysis of the bubble breakup criterion, BBA. Finally, the model is tested in terms of activation of the diffusion term in the α_g -equation (10). The rest of the numerical setup is similar to that used in the Froude number sensitivity study, see Section 5.1.

We restrict the analysis to α_{air} profiles in the uniform flow region. For the u_r model, three values of the bubble radius r_b are considered, along with setting u_r to 0. The result is shown in Fig. 6a. Clearly, including u_r leads to reduced air entrainment, and this effect becomes larger when the input bubble radius is increased. This is expected, since u_r is, by definition, directed upwards.

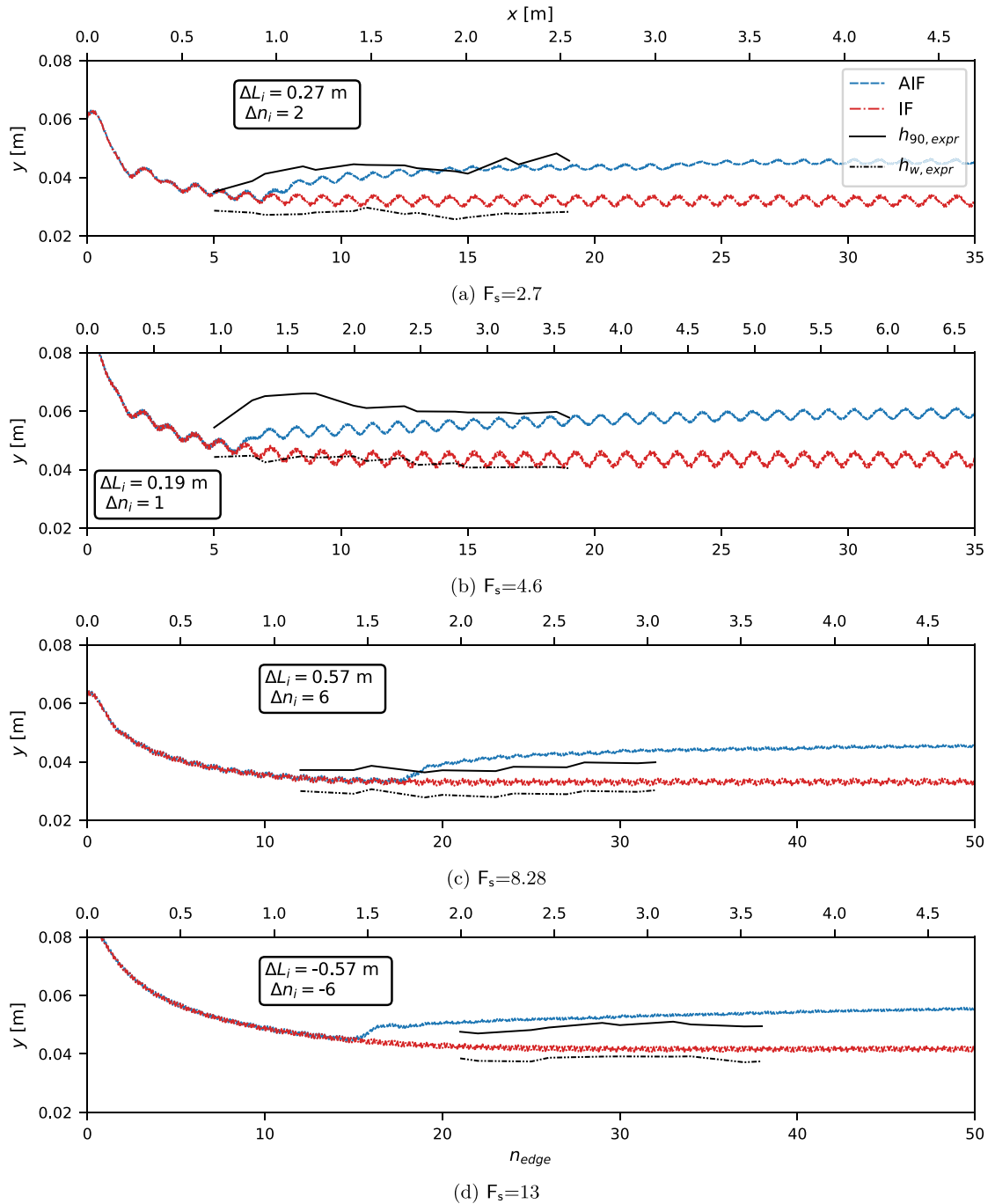


Fig. 3. Surface elevation plots, h_{90} . Stepped spillway flows with different Froude numbers simulated by AIF on the coarsest grid G1, compared to IF simulations and physical model results by Bung [10]. The difference from the experimentally measured inception point is annotated in meters (ΔL_i) and in steps (Δn_i).

The expression for u_r is an important component of the model, but unfortunately it is overshadowed by the uncertainties due to the formulation of δ_{fs} . As demonstrated in the grid sensitivity study, δ_{fs} is currently not defined robustly, and the amount of entrainment heavily depends on the grid. This makes proper calibration of u_r difficult, and has to be left as a future step in the model's development.

Three values of the BBA are considered. The first is 0.1, which is recommended by Lopes et al. [25], and the other two are 0.05 and 0. Recall that the chosen value refers to the minimal volume fraction of water for which α_g is allowed to be

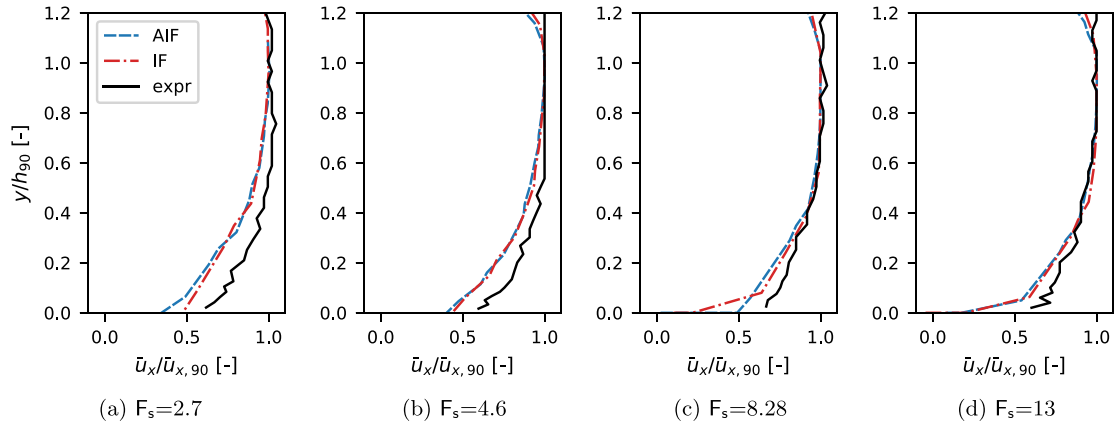
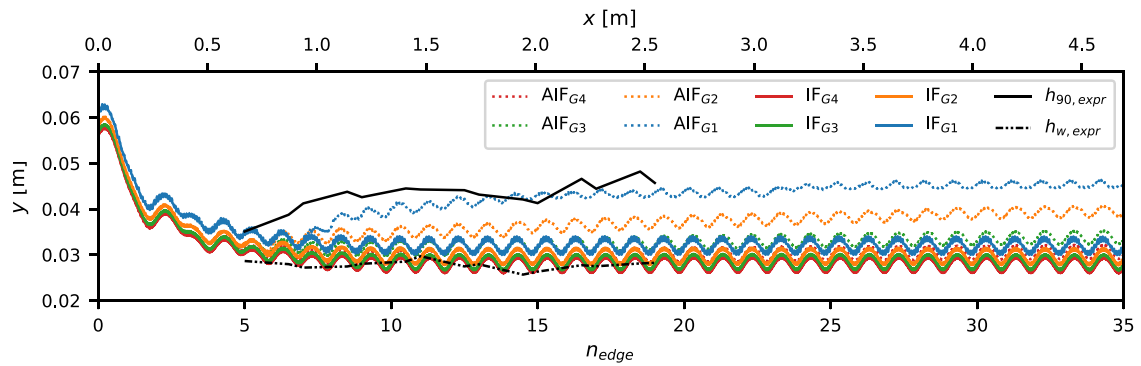


Fig. 4. Vertical profiles for the streamwise velocity for uniform flow conditions. AIF and IF simulation results compared to experimental results by Bung [10].



(a) Surface elevation plot, h_{90} -surface.

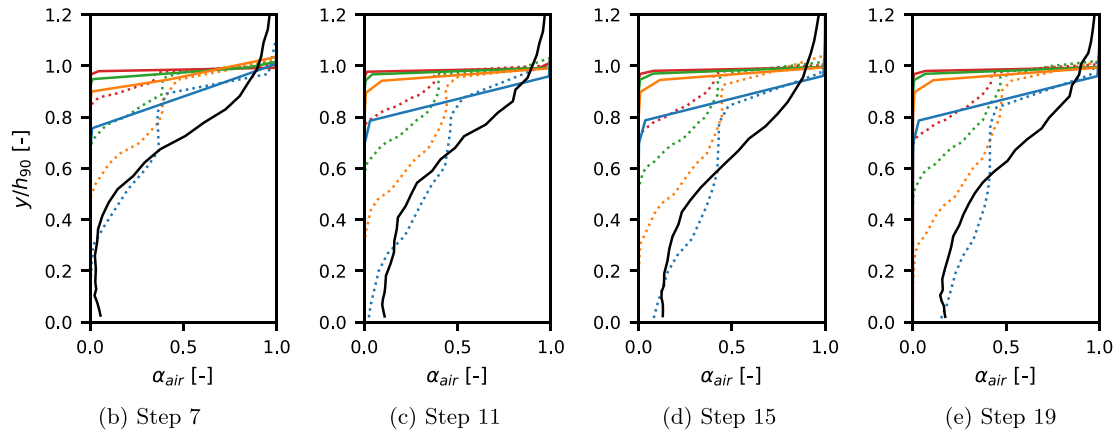


Fig. 5. AIF simulations for $F_s=2.7$ at different grids (G1–G4, G1: $\Delta x = 0.005\text{m}$, G2: $\Delta x = 0.0025\text{m}$, G3: $\Delta x = 0.00125\text{m}$, G5: $\Delta x = 0.000625\text{m}$) compared to physical model results by Bung [10]. Fig. 5a shows the surface elevation, Figs. 5b–5e void fraction profiles for different steps.

non-zero. The results from the three simulations are shown in Fig. 6b. As expected, slightly more air is entrained close to the h_{90} when the BBA value is reduced. Note that compared to the experimental data, the air fractions predicted by AIF close to the interface (from $y/h_{90} \approx 0.8$) are too low. Thus, deactivating the BBA-criterion produces a small improvement in the accuracy meaning that this parameter can be safely removed from the formulation of the model.

Finally, the effect of the diffusion term in (10) is investigated. Two simulations, with and without the diffusion term included, have been conducted, see Fig. 6c. The effect of the diffusion appears to be completely negligible, meaning that, in

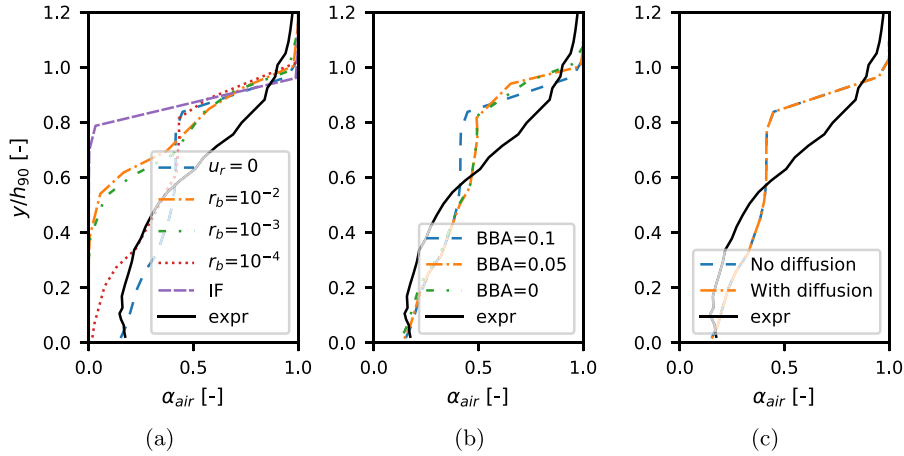


Fig. 6. Sensitivity of α_{air} profiles to the slip velocity model, bubble breakup criterion, and α_g -diffusion.

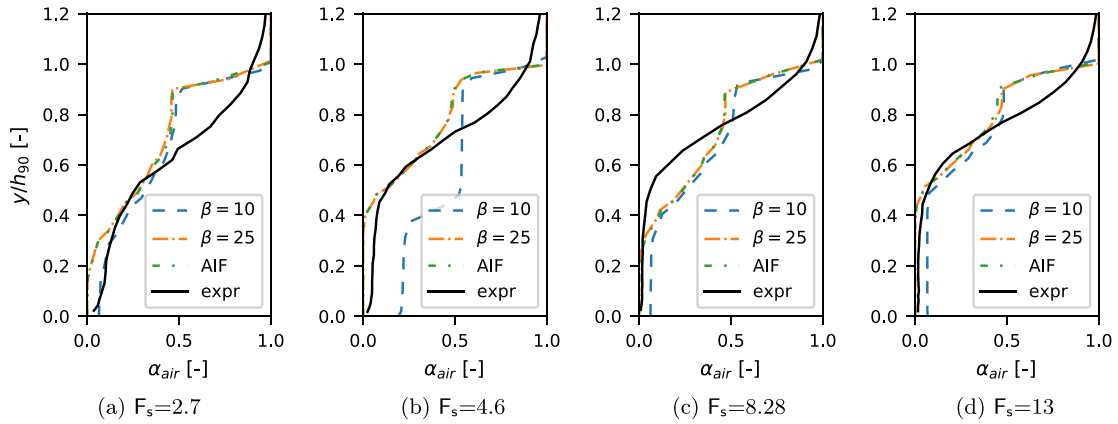


Fig. 7. Sensitivity on β for AIF evaluated on grid G2 for different step Froude numbers. Vertical α_{air} profiles are shown. The data is extracted from what should be the start of the uniform flow region according to the experimental data [10].

practice, it could also be removed. However, this raises a concern since from a physical standpoint mass diffusivity should play a role in the distribution of air.

5.4. Sensitivity to β

As shown in Section 5.2, at high grid resolutions the effects of the model become negligible, or even deactivated. The most important controller of the breadth of the region (in terms of $\nabla\alpha_l$) where entrainment is introduced is the form of δ_{fs} , see Eq. (9). In particular, the parameter β determines the breadth of the tanh function, meaning that with smaller β the region of the model activation becomes larger. In principle, it may thus be possible to maintain an appropriate level of entrainment at high grid resolutions by adjusting β accordingly. However, for this to be possible in practice, the necessary change to β should be easy to predict a priori.

Multiple simulations across different Froude numbers and grid resolutions have been conducted in an attempt to determine whether clear guidelines for setting β could be established. Unfortunately, these efforts were fruitless, and the results of using a given β value change significantly depending on the flow and parameters of the simulation.

As an illustrative example, Fig. 7 shows the α_{air} profiles produced using $\beta = 10$ and 25 in simulations at different Froude numbers on the G2 grid, and compares it to the corresponding profile produced by AIF, where a β -value of 100 is used as default. For $F_s = 2.7$ the sensitivity to β is rather small, but for $F_s = 4.6$ a significant increase in aeration occurs. For larger Froude numbers a lower β mainly leads to more air being present in the corner of the steps. While the change in the α_{air} profiles appears to be rather small, uniform flow conditions are not reached, and its effect continues to grow further downstream. Changes in other simulation parameters also introduce unpredictable changes with respect to the sensitivity of the results to β . For example, contrary to what is observed when using the G2 grid, using G3 instead leads to the $F_s = 2.7$ case becoming very sensitive β .

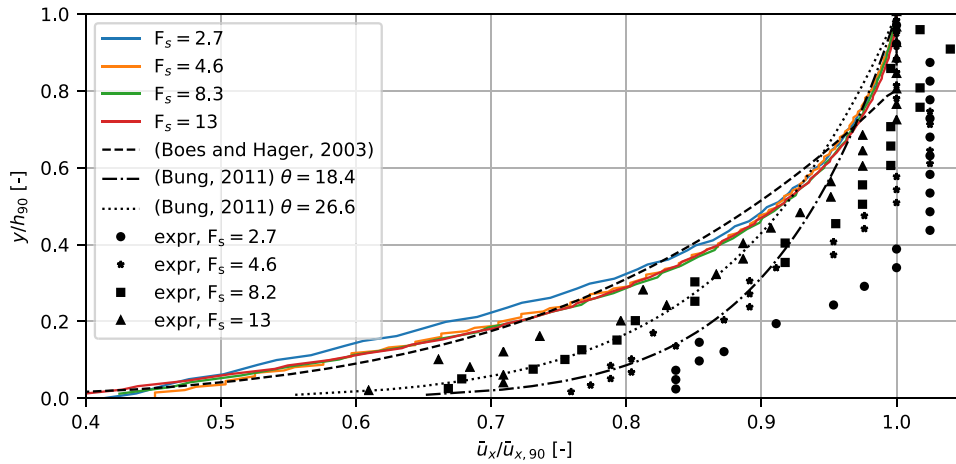


Fig. 8. Normalized streamwise velocity profiles at different Froude numbers, uniform conditions. Power-law estimates from [8] and [10] plotted with non-solid lines. Markers show experimental data from [10].

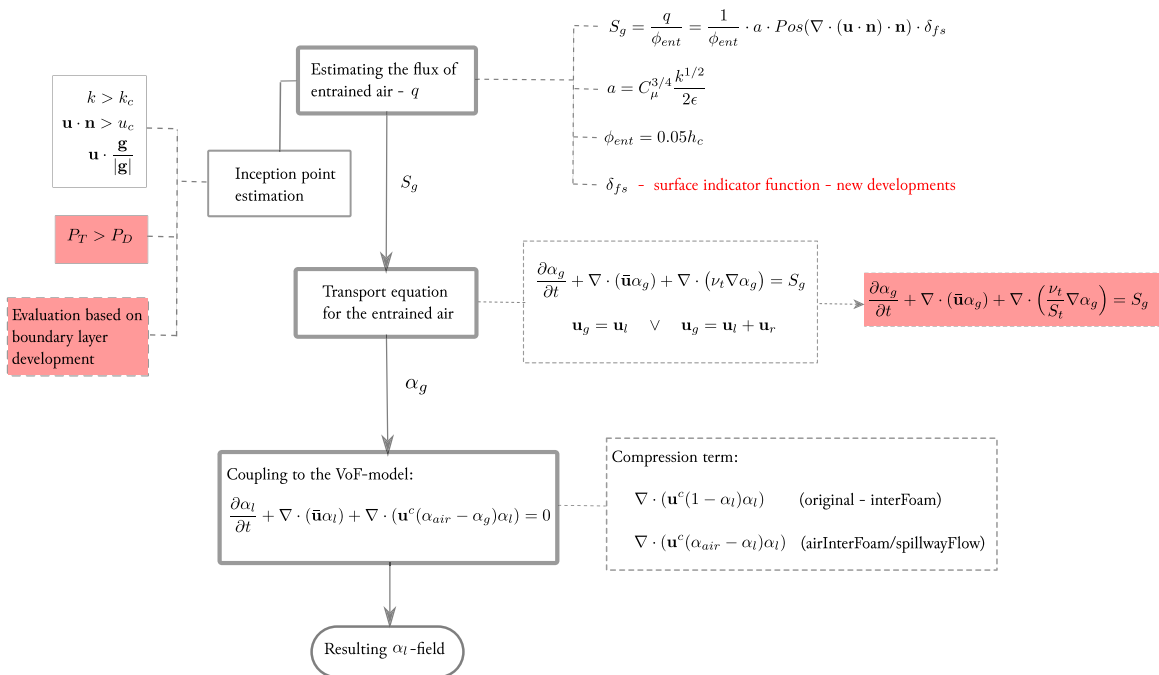


Fig. 9. Outline of the air entrainment model. New developments coloured in red. (For interpretation of the references to colour in this figure legend, the reader is referred to the web version of this article.)

6. Analysis of mean velocity profiles

Both [8] and [10] propose power-law approximations for the form of the streamwise mean velocity profile:

$$\frac{\bar{u}_x}{\bar{u}_{x,90}} = a \left(\frac{y}{h_{90}} \right)^{1/n}. \quad (16)$$

Bung [10] sets $a = 1$ and considers n to be a function of θ . The values $n = 11$ and $n = 8$ are proposed for $\theta = 18.4$ and $\theta = 26.6$, respectively. Boes and Hager [8] use $a = 1.05$ and $n = 4.3$ but consider the estimate to be valid up to $y/h_{90} = 0.8$ after which a flat profile $\bar{u}_x/\bar{u}_{x,90} = 1$ is set.

Fig. 8 shows the velocity profiles obtained in IF simulations on grid G4, together with the estimates above and experimental data [10]. The simulations are conducted with the standard implementation of the $k - \omega$ SST model. Clearly, the power law proposed by Boes and Hager provides a better fit. This is particularly interesting in light of the fact that the simulations reproduce flows from Bung's work [10], i.e. the same article where he introduces his estimates. Note that all the

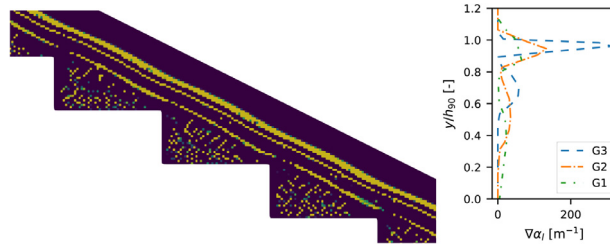


Fig. 10. Left: Typical distribution pattern of an unrestricted S_g . Right: Typical profiles of the gradient of α_l .

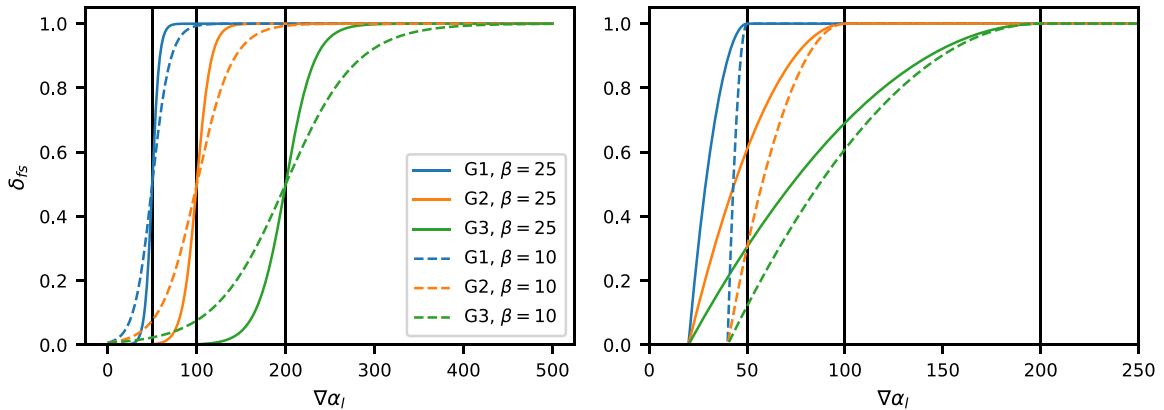


Fig. 11. Surface indicator functions δ_{fs} (17).

profiles for $\theta = 18.4$ collapse perfectly, whereas the profile for $\theta = 26.6$ ($F_s = 2.7$) slightly stands out. Thus, the dependency of the power law on θ does appear to manifest itself. The experimental data is quite scattered but provides stronger support for the estimate of Bung with $n = 11$.

7. Proposed model developments

In the previous sections, two issues with the entrainment model proposed by Lopes et al. [25] have been identified. Perhaps the most critical one is the gradual deactivation of the model upon grid refinement. The other one is the difficulty in prescribing the k_c value in order to get a good prediction of the inception point. In this section, improvements to the model are proposed aiming at alleviating these problems. First, an alternative formulation for the δ_{fs} function is introduced in Section 7.1. Afterwards, amplification of the diffusion term in the α_g is argued for in Section 7.2. Finally, different ways of predicting the inception point is discussed in Section 7.3. Fig. 9 illustrates the air entrainment model, highlighting the developments introduced within this work.

7.1. Free surface detection

Before discussing the formulation of δ_{fs} , it is necessary to consider what kind of restriction of S_g in space is needed in the case of stepped spillway flow. A typical distribution of an unrestricted S_g is shown in the left plot of Fig. 10. The first thick yellow line is located right below the interface and represents the region where the entrainment can be expected to take place. However, a discontinuous strip of non-zero values is also observed close to the pseudo-bottom along with more or less randomly distributed points of activation in the corners of the steps. Physically, no entrainment can occur in these regions, and the δ_{fs} function should filter them out. Note that the spatial separation between the correct and non-physical regions of source term activation is not large, which explains why defining δ_{fs} in a universal way that fits all flow conditions and numerical settings is not trivial.

To arrive at a better formulation for δ_{fs} , it is important to clearly understand the deficiencies of the original definition, see Eq. (9). With $\nabla\alpha_{l,cr}$ set to $1/(4\Delta x)$, the distribution of δ_{fs} over $\nabla\alpha_l$ depends on two quantities: β and Δx . It is instructive to see how δ_{fs} changes shape when the values of these parameters are changed. In the left plot of Fig. 11, $\delta_{fs}(\nabla\alpha_l)$ is shown for Δx values corresponding to grids G1–G3, and the two values of β considered in the sensitivity study in Section 5.4. The tanh function defining the transition region of δ_{fs} from 0 to 1 is centred at $\nabla\alpha_{l,cr}$, shown in the figure with black vertical lines. As the grid is refined, this location is shifted to the right, and for larger values of β , the tanh only spans a limited range of high $\nabla\alpha_l$ values. On the other hand, for smaller β , the tanh becomes so wide that δ_{fs} remains non-zero everywhere.

This behaviour of δ_{fs} should be related to how $\nabla\alpha_l$ is typically distributed across y , see the right plot in Fig. 10. Note that the high values of $\nabla\alpha_l$ are always restricted to a relatively thin region close to the interface. Consequently, for a large β , for example $\beta = 100$ as proposed in [25], δ_{fs} will be restricted to an increasingly smaller region in space when the grid gets refined. This explains why the diminishing effect of the entrainment with grid refinement observed in Section 5.2.

As mentioned above, it is easy to make the δ_{fs} function less restrictive by lowering β . However, the issue here is that the β and the effective cut-off value in terms of $\nabla\alpha_l$ are not intuitively related. This is problematic given that the margin of error is quite small, as discussed above in relation to the typical distribution of S_g .

Alternative options for the expression of δ_{fs} were explored, including a parabola based function, and a step-shaped function defined purely based on the distance from a defined interface. For both alternatives, the idea was to set the value of the critical gradient of α_l relatively tight, to capture the upper peak in the gradient plot in Fig. 10, and then expand its prevalence away from these locations according to an appropriate function or logic. In the distance based alternative, δ_{fs} was set to 0 or 1 for a particular cell, depending on its distance from the defined interface. If this distance was less than the interface thickness, ϕ_{ent} , δ_{fs} was set to 1, and otherwise its value was set to 0. However, this led to step-shaped profiles of α_l , where too much air was entrained below the interface, and indicated a need to apply some functionality to reduce the effects of the source term as the gradient of α_l is reduced below its critical value.

Acknowledging the above, a parabola based function was considered. The possibility to define $\nabla\alpha_{cr}$ as a top point of the function, and to define a cut-off value for the gradient as an intersection point, was viewed as beneficial features of this function in the current setting. The latter leads to the possibility of avoiding the long tail in the tanh-function, with the corresponding uncontrollable potential for generation of non-zero values of S_g within the steps. The parabola-based δ_{fs} formulation is proposed as

$$\delta_{fs}(\nabla\alpha_l) = \begin{cases} \text{Pos}\left(-\frac{1}{4d}\left(|\nabla\alpha_l| - |\nabla\alpha_{l,cr}|\right)^2 + 1\right) & \text{if } \nabla\alpha_l < |\nabla\alpha_{l,cr}| \\ 1 & \text{otherwise.} \end{cases} \quad (17)$$

Here, d refers to the distance from the vertex of the parabola to its focus, which can be computed as

$$d = 0.25\left(|\nabla\alpha_{l,cr}| - |\nabla\alpha_{l,cut}|\right)^2,$$

where $\nabla\alpha_{l,cut}$ is an input parameter explicitly defining the lowest $\nabla\alpha_l$ for which the source term may assume non-zero values. The proposed δ_{fs} , computed for grids G1-G3 and two different values of $\nabla\alpha_{l,cut}$, is shown in the right plot of Fig. 11. The non-zero values of the function are always fixed to the interval $[\nabla\alpha_{l,cut}, \nabla\alpha_{l,cr}]$, which expands upon grid refinement. Unfortunately, due to this expansion, even with this new δ_{fs} , the region of non-zero S_g values shrinks as the grid is refined. However, the process is slowed, since δ_{fs} is left to be non-zero at lower $\nabla\alpha_l$.

During initial testing, it was observed that the parabola-based δ_{fs} was very effective at filtering out the sporadic source term activation in the corner of the steps, while preserving the region where entrainment is expected. However, the secondary strip of non-zero S_g values close to the pseudobottom (see left plot in Fig. 10) would sometimes still be left unfiltered. This is likely related to the secondary peak in $\nabla\alpha_l$. To rectify this, the parabolic surface indicator function in Eq. (17) is combined with a distance based approach like the one outlined above.

In details, the values of δ_{fs} computed according to Eq. 17 are additionally manipulated as follows. First, the cells in which $\delta_{fs} \geq 0.9$ are selected. These should lie near the interface and are therefore likely to belong to the region where S_g should be activated. For the remaining cells, the distance to the nearest cells with $\delta_{fs} \geq 0.9$ is computed. If this distance exceeds the interface thickness, ϕ_{ent} , the value of δ_{fs} in the cell is set to 0. Overall, this combined formulation gave improvements compared to the original formulation based on tanh. It is noted that even without the distance cut-off modification, improved results with the parabolic δ_{fs} could be achieved, and the $\delta_{fs} \geq 0.9$ criterion can give false positives.

Finally, making both $\nabla\alpha_{l,cr}$ and $\nabla\alpha_{l,cut}$ grid independent parameters has briefly been tested, but abandoned due to the sensitivity of the results to the chosen values. In general, our extensive efforts and experimenting with δ_{fs} formulations and other simulation settings showed that constructing a robust and accurate δ_{fs} is very challenging. The sensitivity of the results to any changes in the simulation parameters or flow conditions tends to be very strong. Nevertheless, as shown in the Section 8, the proposed δ_{fs} does represent an improvement with respect to prior art.

7.2. Modelling air propagation into the corners of the steps

By definition, the employed entrainment model is meant to account for aeration occurring close to the free surface, within some layer of thickness ϕ_{ent} . However, experimental results clearly show that in the case of the stepped spillway, air penetrates all the way down to the surface of the steps, see e.g. the experimental profiles in Fig. 2. The physical mechanism through which this occurs is described by Pfister and Hager [11]. Inspection of video recordings from their experiments reveals the occasional generation of air troughs that extend from the surface into the bulk flow. These troughs penetrate deep enough to hit the step edges, and when they do, the air is distributed into the steps.

Capturing this intrinsically transient process in a steady state model is not straightforward. Here, we consider using a somewhat ad-hoc approach, taking advantage of the diffusion term in the α_g equation (10), $\nabla \cdot (\nu_t / Sc \nabla \alpha_g)$. Recall that in Section 5.3 it was shown that the effect of this term on the solution is essentially negligible. However, the effect can be easily amplified by adjusting Sc .

The increased diffusion of α_g will then lead to air being redistributed more evenly across y , and consequently result in stronger aeration closer to the pseudo-bottom.

The difficulty lies in the choice of the value of Sc since there is no clear physical analogy between the modelled phenomenon and diffusion. In light of this, it was attempted to search for a suitable value through experimentation, to see whether one leading to improved results across all the considered Froude numbers could be found. As a result, $Sc = 1/150$ was selected.

7.3. Inception point prediction

Even if AIF predicts the aeration onset correctly when appropriate values for k_c and u_c are supplied, the inception point estimation using this method completely depends on user input. As shown in Section 5.1, the appropriate critical value k_c depends on the flow conditions.

In an effort to improve the reliability of predictions, two alternative approaches are considered. One, found in the work of Hirt [20], is based on the balance between the energy of turbulent motion and that of gravity and surface tension. Defining

$$P_t = \rho k, \quad (18)$$

$$P_d = \rho |g| a + \frac{\sigma}{a}, \quad (19)$$

the source term S_g is activated only in cells where $P_t > P_d$. This way the inception point prediction requires no further user input. However, it completely relies on the correct prediction of the turbulent kinetic energy, k , and the turbulent length scale, a , at the interface. Unfortunately, conventional RANS models are known for not being able to do that accurately, and over-prediction of the turbulent viscosity near the interface is a known issue. Remedies have been proposed (see e.g. [42]), but shall not be investigated here.

Another estimation approach is based on the development of the turbulent boundary layer formed along the pseudo-bottom. As mentioned in the introduction, the intersection of the boundary layer with the free surface is traditionally considered to trigger air entrainment. Thus, an estimate of the location of the interception can serve as an estimate of the inception point.

The location of the interface is readily approximated with h_{90} , so the problem boils down to computing the boundary layer thickness. A typically used measure is δ_{99} , which is the location at which $\bar{u}_x = 0.99\bar{u}_{x,90}$. It should be appreciated that due to the flatness of the velocity profile near the edge of the boundary layer, this measure is prone to contamination even by small differences in the obtained velocity values. For the same reason, δ_{99} is not a very close measure of δ .

An advantage of the flow in a spillway is that, sufficiently downstream, δ stops growing and remains $\approx h_{90}$, since the boundary layer in the water does not penetrate the interface. (Instead, a separate boundary layer is formed in the air phase, see Fig. 2 in [5]). This means that if we assume that the boundary layer is self-similar under the scaling with δ_{99} and $\bar{u}_{x,90}$, its intersection with h_{90} is readily obtained as the point where δ_{99} reaches its value at uniform conditions. Put differently, we seek the onset of self-similarity with respect to scaling with h_{90} and $\bar{u}_{x,90}$.

To conclude, it is pointed out that both of the considered methods can be applied to the baseline VoF solution, prior to the simulation employing the entrainment model. For the case of the boundary layer-based estimate, this is possible in light of the observed insensitivity of the velocity profiles to the air entrainment. The $P_t > P_d$ estimate simply does not rely on data downstream of the inception of entrainment.

8. Simulations with the modified model

This section is dedicated to evaluating the effects of the model improvements proposed above. To that end, a new solver incorporating these changes has been implemented. Reflecting the focus on stepped spillway simulations, the solver is called *spillwayFlow*², which is abbreviated to SPF below. The robustness of the model with respect to grid resolution is evaluated in Section 8.1. Results from application of the model to stepped spillway flow at all four considered Froude numbers are presented Section 8.2. The proposed criteria for inception point location are tested separately, in Section 8.3.

8.1. Grid sensitivity

Here the new model is put to the same grid sensitivity analysis as presented in Section 5.2 for AIF. To simplify the analysis, the new inception point prediction approach is not employed, and the original criterion based on k_c is used instead. Simulation results for the $F_s=2.7$ case obtained on grids G1–G4 are shown in Fig. 12. Here, the diffusion term in the α_g equation is thus inactive. As anticipated, the results still depend on the grid, and the general trend is convergence towards the IF solution. Note that in the α_{air} profiles, the reduction of aeration manifests itself predominately at $y/h_{90} \lesssim 0.6$. Closer to h_{90} results remain acceptable even on the G4 grid. Related to the absence of air in the lower parts, the predictions of h_{90}

² <https://github.com/siljekre/spillwayFlow>

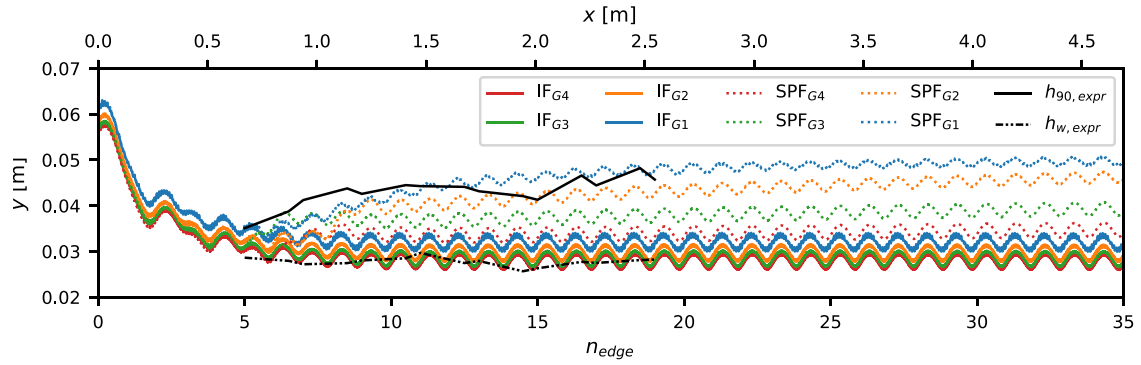
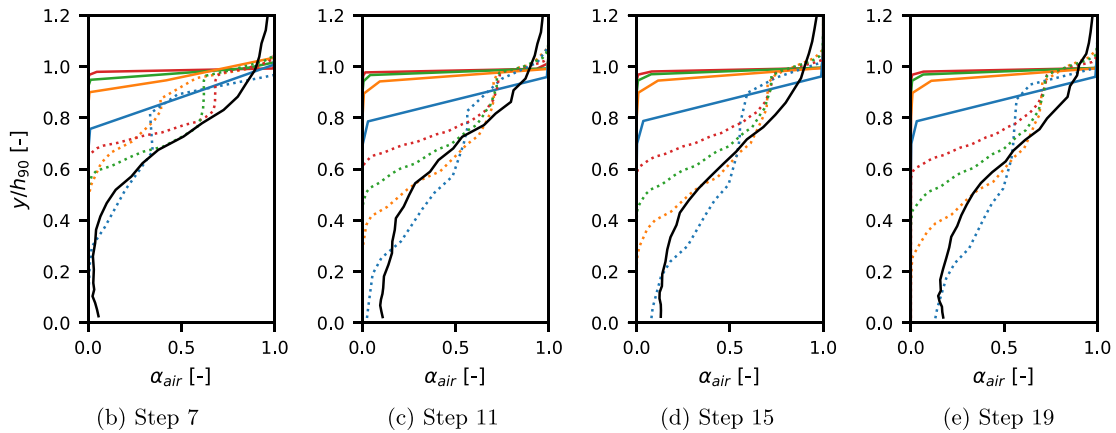
(a) Surface elevation plot, h_{90} -surface.

Fig. 12. SPF simulated with no α_g -diffusion and $F_s=2.7$ at different grids (G1–G4, G1: $\Delta x = 0.005\text{m}$, G2: $\Delta x = 0.0025\text{m}$, G3: $\Delta x = 0.00125\text{m}$, G5: $\Delta x = 0.000625\text{m}$) compared to physical model results by Bung [10]. Fig. 12a shows the surface elevation, Figs. 12b–12e, the void fraction profiles at different steps.

itself are more sensitive, and unfortunately on the finer grids the accuracy is poor. Nevertheless, compared to the original AIF results (see Fig. 5) the robustness of the model is improved.

Fig. 13 shows the results obtained with $Sc = 1/150$. As expected, a comparatively more even distribution of α_{air} across y is achieved, in particular for the simulations on denser grids. Furthermore, a very clear improvement in the robustness of the model is evident, with much more similar results obtained on all four grids.

8.2. Results for different Froude numbers

Now, the results obtained with the new model are presented for all four considered values of the Froude number. The simulations were run on the densest mesh, G4. As in the section above, the new criterion for locating the inception point is not used here, and instead k_c is adjusted for each case in order to match the location in the experimental data. For completeness, profiles corresponding to both no α_g -diffusion and $Sc = 1/150$ are shown in all the figures. For comparison, they also include results from AIF simulations on the G1 grid, and also from IF simulations on the G4 grid.

The α_{air} profiles are discussed first, see Fig. 14. Qualitatively, the same behaviour with respect to α_g -diffusion is observed for all F_s . With no diffusion the distribution of α_{air} across y is close to step-wise, with decent agreement with experimental data for $y/h_{90} \gtrsim 0.7$. When $Sc = 1/150$, the profiles are smoothed out, which generally increases the accuracy. The exception is the $F_s=8.28$ case, for which the air volume fraction at low y/h_{90} becomes excessive. Yet even for this case the agreement is better than what could be achieved with AIF.

The surface elevation plots are shown in Fig. 15. Overall, $Sc = 1/150$ leads to better results, which agree well with the experimental data in the uniform flow region. An interesting exception is the $F_s=4.6$, for which Sc barely has influence on h_{90} in the uniform flow region, whereas in the developing region not including the diffusion term leads to very good agreement with the experiment. However, it is unlikely that this is explained by any fundamental property of the flow or the model. Compared to AIF, the accuracy of the new model is generally on par. AIF curves are marginally closer to experimental data for the two lower F_s , and the other way around for the two higher F_s .

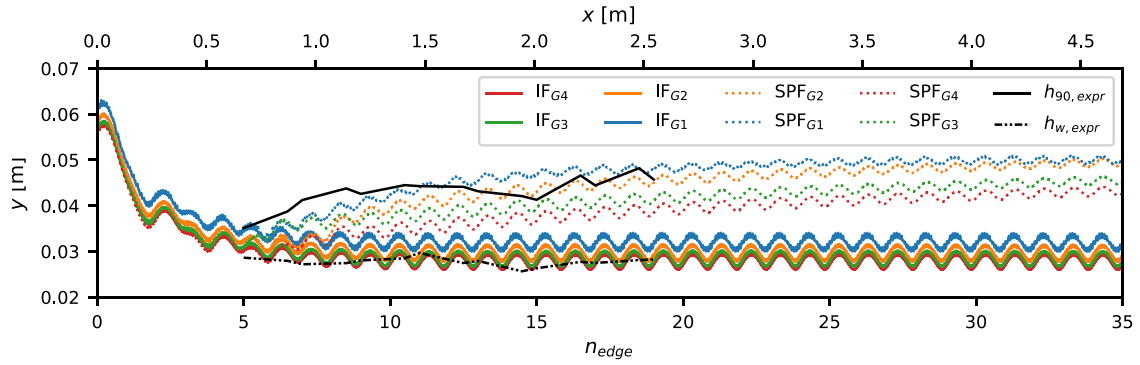
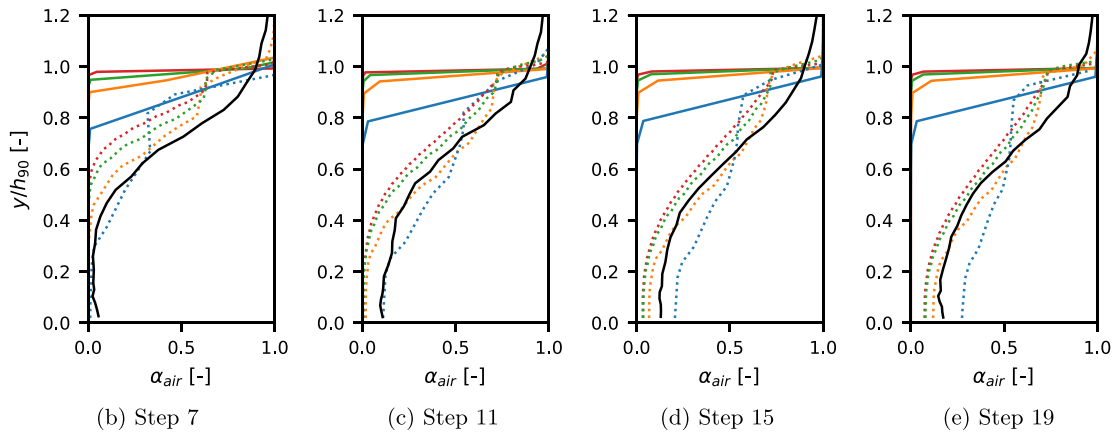
(a) Surface elevation plot, h_{90} -surface.

Fig. 13. SPF simulated with α_g -diffusion ($Sc = 1/150$) and $F_s=2.7$ at different grids (G1–G4, G1: $\Delta x = 0.005m$, G2: $\Delta x = 0.0025m$, G3: $\Delta x = 0.00125m$, G5: $\Delta x = 0.000625m$) compared to physical model results by Bung [10]. Fig. 13a shows the surface elevation, Figs. 13b–13 e, the void fraction profiles at different steps in the developing region.

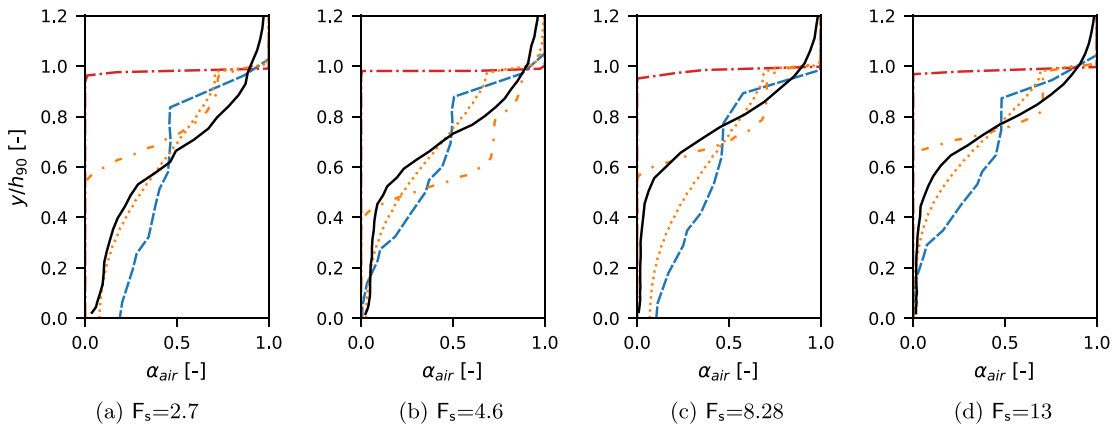


Fig. 14. Vertical void fraction profiles for uniform flow conditions. Stepped spillway flows at different Froude numbers. SPF simulations (G4) compared to IF (G4), AIF (G1) and experimental results by Bung [10]. All plots are showing profiles at step edges.

8.3. Inception point analysis

In this section, the inception point estimation criteria presented in Section 7.3 are tested. Anticipating the influence of turbulence modelling, the estimates are based on IF solutions obtained with $k - \omega$ SST and the respective counterpart in the library by Fan and Anglart [34], in which the density gradient is properly accounted for in the transport equations.

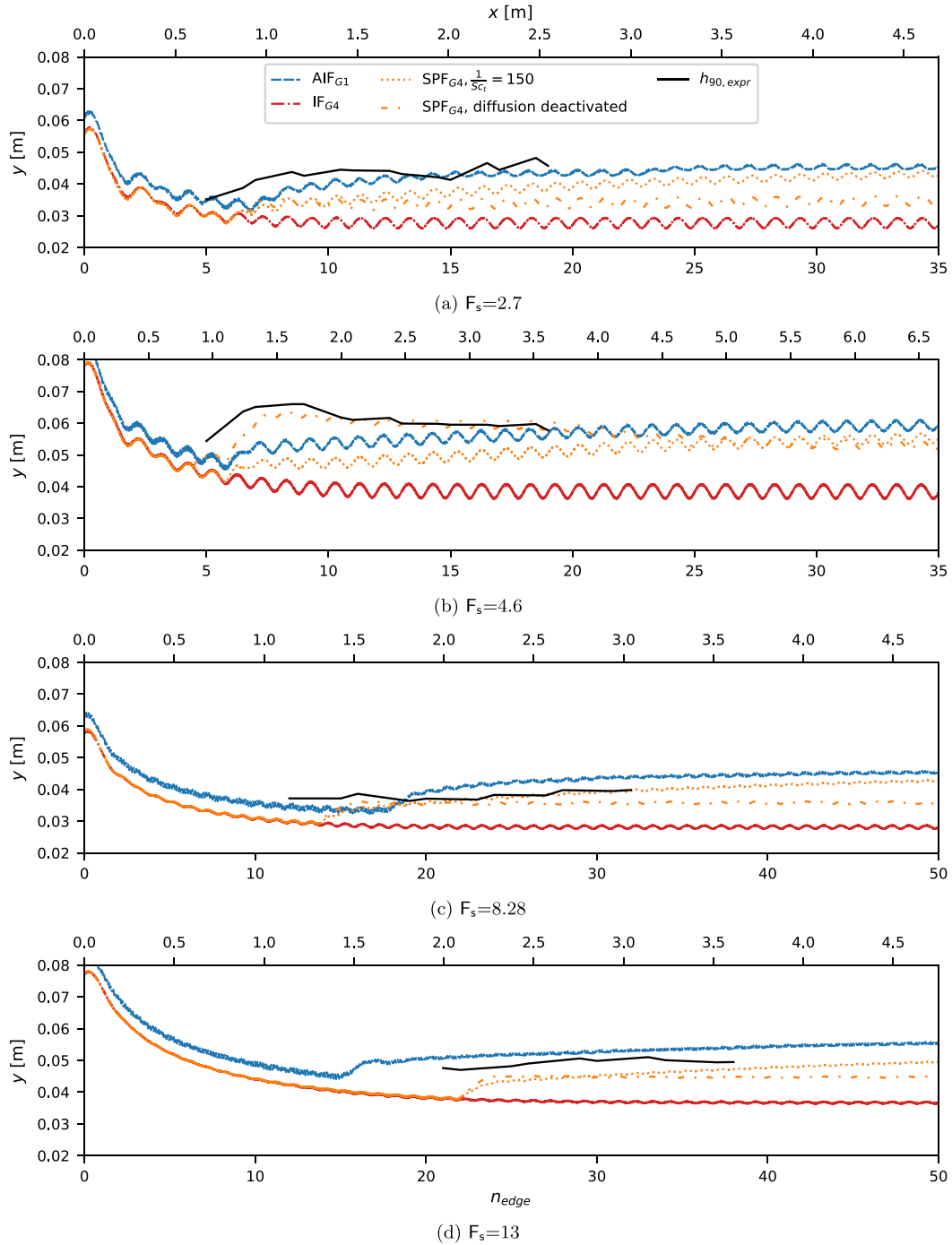


Fig. 15. Surface elevation plots, h_{90} . Stepped spillway flows at different Froude numbers. SPF simulations (G4) compared to IF (G4), AIF (G1) and experimental results by Bung [10].

All simulations are performed on the G3 grid, which is sufficiently dense for the velocity and turbulent quantities to be converged.

The results based on the growth of δ_{99} are shown in Fig. 16. No significant influence of the turbulence model is observed. As expected, some oscillations in the values are visible as the curves flatten out. Typically, the inception point can then be estimated as the location where such oscillations begin to take place. Some cases may be tricky, however; for example, $F_s=4.6$ simulated with the standard $k-\omega$ SST. Here, δ_{99} continues to grow monotonously towards the last step. In this

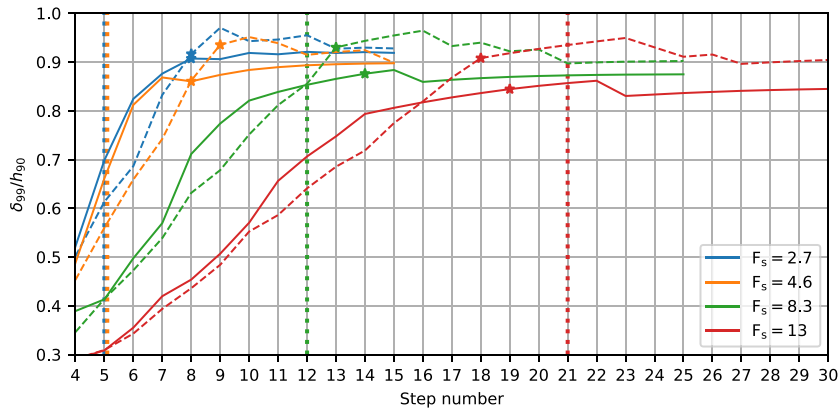


Fig. 16. Development of δ_{99} along the pseudo-bottom. Solid lines show results for the standard $k - \omega$ SST, and dashed lines for the implementation by Fan and Anglart [34]. Stars show the estimated location of the inception point. Dotted vertical lines show the inception point location registered in the reference experiment [10].

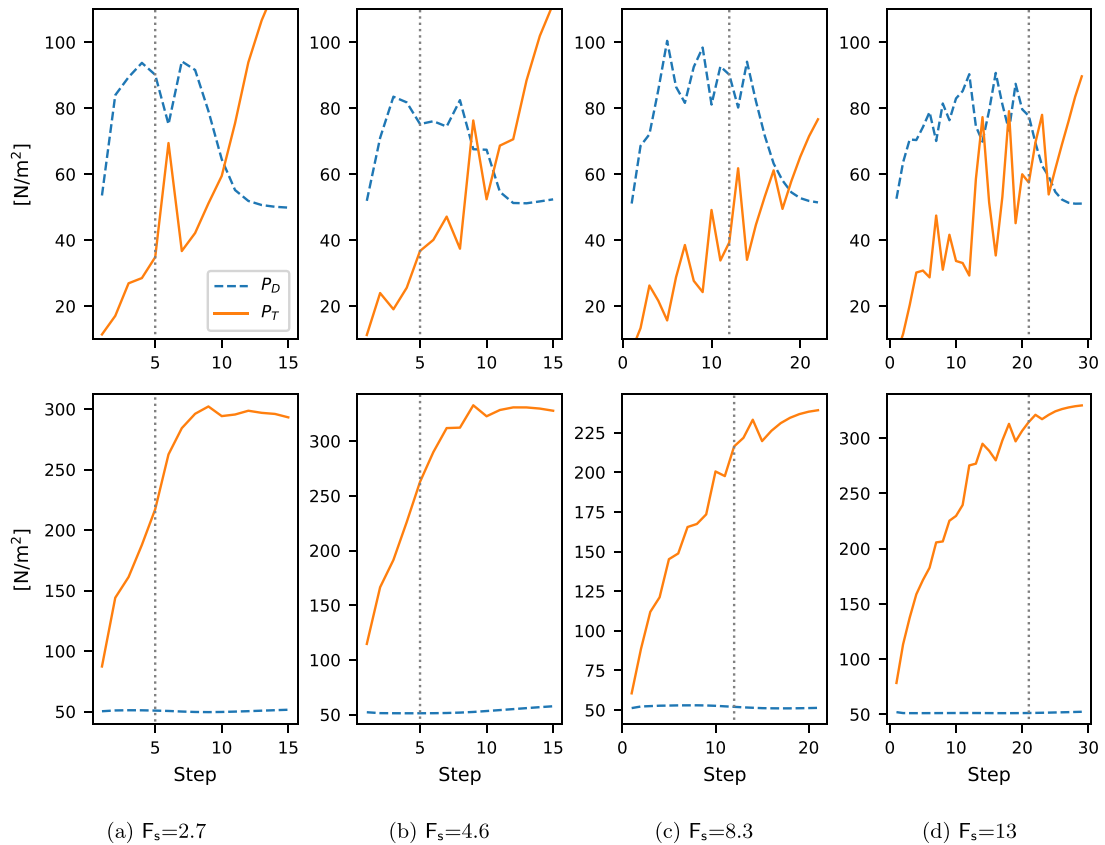


Fig. 17. Test of Pt-Pd criterion for inception point for the different F_s -cases. Plotted for step niches for the isoline $\alpha_l = 0.5$. Standard $k - \omega$ SST (bottom), modified version by Fan and Anglart [34] (top). Grid resolution G3. The vertical dotted lines indicate experimental results [10].

case, it is possible to look at the velocity profiles and try to find the location where self-similarity is obtained with respect to scaling with h_{90} and $\bar{u}_{x,90}$. Excluding one case, the predictions disagree with the experimental data by at most 3 step lengths. The corresponding values in meters can be found in Table 3.

We note also that the value of δ_{99} in uniform conditions lies between 0.85 and 0.92. Thus, a less accurate estimation of the inception point can be made without having to obtain the velocity profile downstream by simply assuming the threshold value to be $\delta_{99} \approx 0.9$.

Table 3

Inception point locations, L_i , found using the energy balance equations (18)–(19) and the boundary layer thickness. IF simulations on grid G3 using two different turbulence models. Comparison to experimental results by Bung [10]. Numbers given in [m].

F_s	Turbulence	$L_{i,expr}$	$L_{i,\delta_{99}}$	$\Delta L_{i,\delta_{99}}$	$L_{i,P_1 > P_d}$	$\Delta L_{i,P_1 > P_d}$
2.7	$k - \omega$ SST	0.7	1.1	0.4	–	–
2.7	$k - \omega$ SST, varRho	0.7	1.1	0.4	1.3	0.6
4.6	$k - \omega$ SST	1.0	1.5	0.5	–	–
4.6	$k - \omega$ SST, varRho	1.0	1.7	0.7	1.7	0.8
8.2	$k - \omega$ SST	1.1	1.3	0.2	–	–
8.2	$k - \omega$ SST, varRho	1.1	1.2	0.1	1.7	0.6
13	$k - \omega$ SST	2.0	1.8	–0.2	–	–
13	$k - \omega$ SST, varRho	2.0	1.7	–0.3	1.4	–0.6

The results for the energy balance-based approach are shown in Fig. 17. The selection of the turbulence model has a very large influence on the results, which is unsurprising. Unfortunately, for the standard implementation of $k - \omega$ SST inception is predicted directly at the inlet. The variable density modification [34] improves the results significantly, but they still remain inferior to those provided by the δ_{99} -based approach.

All the obtained estimates and corresponding errors with respect to experimental data can be found in Table 3. Since the δ_{99} -based approach proved to be more accurate and robust, it is generally the recommended choice.

9. Conclusions

This study presents developments in numerical modelling of self-aeration in stepped spillways. The model of Lopes et al. [25] is taken as baseline, and a large simulation campaign is conducted in order to explore its properties: robustness with respect to flow conditions, grid resolution, as well as sensitivity to the model parameters. The simulations were performed for stepped spillway geometries and inflow discharge values used in the experiments of Bung [10], and cover four step Froude numbers in the range from 2.7 to 13. The corresponding experimental data was used as reference.

The results showed that the model exhibits significant deficiencies, the most stark being its dependency on the resolution on the grid. A complete deactivation of the model was observed when the grid cell size was refined to 1.25 mm. The main reason behind this has been identified to be the form of δ_{fs} , which is the function used for limiting the activation region of the volumetric air entrainment source term, see Eq. (9). The region of non-zero values of δ_{fs} shrinks as the grid gets refined, and, in the limit, the source term is set to zero in the whole domain, regardless of flow conditions.

The above makes it difficult to calibrate the other parameters of the model, such as the bubble rise velocity u_r and the Schmidt number. For $Sc = 1$, turbulent diffusion had no effect on the solution, which raises concerns.

A new formulation for δ_{fs} is proposed here, combining a parabolic profile with distance-based cut-off. Simulations reveal that while fundamentally the results still depend on the grid resolution, under the new definition of δ_{fs} the robustness of the model is improved significantly, and the model remains active on the finest considered grid, with cell size 0.625 mm.

As an additional modification, amplifying the diffusion term in the α_g -equation (10) is proposed in order to account for the propagation of entrained air into corners of the steps. Results reveal that this leads to an improvement in predictive accuracy, the new model performing better than the original [25] across the whole considered range of F_s numbers. Furthermore, the robustness of the model with respect to grid resolution improves significantly as well. It should be acknowledged that the selection of the value of the Schmidt number, $Sc = 1/150$, is currently not physically motivated and can, therefore, be called into question. Nevertheless, we believe that the possibility to use the same value across different flow conditions and the clearly demonstrated advantages in terms of the performance of the model are sufficiently strong arguments in favour of adopting the proposed modification.

The inception point detection algorithm used in [25] relies on a priori knowledge of critical turbulent kinetic energy level. Since this is impractical, two alternative approaches were tested. One is based on energy balance and proposed in [20], and the other is based on the analysis of the turbulent boundary layer development. Both algorithms led to useful predictions. However, the energy-based method revealed high sensitivity to the choice of the turbulence model and failed completely when the standard $k - \omega$ SST model was used (i.e. without the variable-density modification [34].) Excluding those results, the average error across the four considered Froude numbers are 0.35 m and 0.65 m for the boundary layer- and energy balance-based method, respectively. The boundary layer-based approach is thus recommended due to better robustness and improved accuracy.

Finally, analysis of normalized mean velocity profiles showed good collapse across the four considered Froude numbers and agreement with the power law proposed in [8]. An interesting observation is that the velocity profiles seem to be nearly unaffected by the distribution of the fluid's phase.

A clear direction for future work is further improving the formulation of the terms in the α_g -equation: δ_{fs} in the source term, u_r in the convective term, and Sc in the diffusive term. Evaluating the models applicability to other self-aerated flows

is also of interest. A logical first step is to consider a smooth spillway, due to the clear similarities with the stepped counterpart.

Acknowledgments

This work was supported by grant number P38284-2 from the Swedish Energy Agency. The simulations were performed on resources provided by Chalmers Centre for Computational Science and Engineering (C3SE), the NTNU IDUN/EPIC computing cluster, and UNINETT Sigma2 – the National Infrastructure for High Performance Computing and Data Storage in Norway. The authors are thankful to Daniel Bung for sharing the data files from his physical experiments and to Pedro Lopes for sharing the source code of the airInterFoam solver.

References

- [1] D.A. Ervine, H. Falvey, Behaviour of turbulent water jets in the atmosphere and in plunge pools, *Proc. Inst. Civ. Eng.* 83 (1) (1987) 295–314, doi:[10.1680/jicep.1987.353](#).
- [2] L.G. Straub, A.G. Anderson, Experiments on self-aerated flow in open channels, *J. Hydraul. Div.* 84 (7) (1958) 1–35.
- [3] X. Cheng, J. Gulliver, D. Zhu, Application of displacement height and surface roughness length to determination boundary layer development length over stepped spillway, *Water (Basel)* 6 (12) (2014) 3888–3912, doi:[10.3390/w6123888](#).
- [4] G. Zhang, H. Chanson, Hydraulics of the developing flow region of stepped spillways. i: physical modeling and boundary layer development, *J. Hydraul. Eng.* 142 (7) (2016) 04016015, doi:[10.1061/\(asce\)hy.1943-7900.0001138](#).
- [5] D. Valero, D.B. Bung, Development of the interfacial air layer in the non-aerated region of high-velocity spillway flows. instabilities growth, entrapped air and influence on the self-aeration onset, *Int. J. Multiphase Flow* 84 (2016) 66–74, doi:[10.1016/j.ijmultiphaseflow.2016.04.012](#).
- [6] D. Valero, D.B. Bung, Reformulating self-aeration in hydraulic structures: turbulent growth of free surface perturbations leading to air entrainment, *Int. J. Multiphase Flow* 100 (2018) 127–142, doi:[10.1016/j.ijmultiphaseflow.2017.12.011](#).
- [7] D. V. Huerta, On the Fluid Mechanics of Self-Aeration in Open Channel Flows, Université de Liège, Liège, Belgique, 2018 Ph.D. thesis.
- [8] R.M. Boes, W.H. Hager, Two-phase flow characteristics of stepped spillways, *J. Hydraul. Eng.* 129 (9) (2003) 661–670, doi:[10.1061/\(asce\)0733-9429\(2003\)129:9\(661\)](#).
- [9] J. Matos, A.N. Pinheiro, A.C. Quintela, K.H. Frizell, On the role of stepped overlays to increase spillway capacity of embankment dams, in: *Proceedings ICOLD European Symposium Dams in a European Context*, 2001.
- [10] D.B. Bung, Developing flow in skimming flow regime on embankment stepped spillways, *Journal of Hydraulic Research* 49 (5) (2011) 639–648, doi:[10.1080/00221686.2011.584372](#).
- [11] M. Pfister, W.H. Hager, Self-entrainment of air on stepped spillways, *Int. J. Multiphase Flow* 37 (2) (2011) 99–107, doi:[10.1016/j.ijmultiphaseflow.2010.10.007](#).
- [12] R.M. Boes, W.H. Hager, Hydraulic design of stepped spillways, *J. Hydraul. Eng.* 129 (9) (2003) 671–679, doi:[10.1061/\(asce\)0733-9429\(2003\)129:9\(671\)](#).
- [13] J. Roenby, H. Bredmose, H. Jasak, A computational method for sharp interface advection, *R Soc Open Sci* 3 (11) (2016) 160405, doi:[10.1098/rsos.160405](#).
- [14] M. Mortazavi, V.L. Chenadec, P. Moin, A. Mani, Direct numerical simulation of a turbulent hydraulic jump: turbulence statistics and air entrainment, *J. Fluid Mech* 797 (2016) 60–94, doi:[10.1017/jfm.2016.230](#).
- [15] S. Hänsch, D. Lucas, E. Krepper, T. Höhne, A multi-field two-fluid concept for transitions between different scales of interfacial structures, *Int. J. Multiphase Flow* 47 (2012) 171–182, doi:[10.1016/j.ijmultiphaseflow.2012.07.007](#).
- [16] K.E. Wardle, H.G. Weller, Hybrid multiphase CFD solver for coupled dispersed/seggregated flows in liquid-liquid extraction, *Int. J. Chem. Eng.* 2013 (2013), doi:[10.1155/2013/128936](#).
- [17] K. Yan, D. Che, A coupled model for simulation of the gas-liquid two-phase flow with complex flow patterns, *Int. J. Multiphase Flow* 36 (4) (2010) 333–348, doi:[10.1016/j.ijmultiphaseflow.2009.11.007](#).
- [18] J. Ma, A.A. Oberai, D.A. Drew, R.T. Lahey, M.C. Hyman, A comprehensive sub-grid air entrainment model for rans modeling of free-surface bubbly flows, *The Journal of Computational Multiphase Flows* 3 (1) (2011) 41–56, doi:[10.1260/1757-482x.3.1.41](#).
- [19] F. Moraga, P. Carrica, D. Drew, R. Lahey, A sub-grid air entrainment model for breaking bow waves and naval surface ships, *Computers & Fluids* 37 (3) (2008) 281–298, doi:[10.1016/j.compfluid.2007.06.003](#).
- [20] C. Hirt, Modeling turbulent entrainment of air at a free surface, *Flow Science, Inc* (2003).
- [21] D. Valero, D. Bung, Hybrid investigation of air transport processes in moderately sloped stepped spillway flows, in: *E-proceedings of the 36th IAHR World Congress 28 June - 3 July, 2015, The Hague, the Netherlands, 2015*, pp. 1–10.
- [22] Dong, Wang, Vetsch, Boes, Tan, Numerical simulation of air–water two-phase flow on stepped spillways behind x-shaped flaring gate piers under very high unit discharge, *Water (Basel)* 11 (10) (2019) 1956, doi:[10.3390/w11101956](#).
- [23] F.A. Bombardelli, I. Meireles, J. Matos, Laboratory measurements and multi-block numerical simulations of the mean flow and turbulence in the non-aerated skimming flow region of steep stepped spillways, *Environ. Fluid Mech.* 11 (3) (2010) 263–288, doi:[10.1007/s10652-010-9188-6](#).
- [24] A. Bayon, J.P. Toro, F.A. Bombardelli, J. Matos, P.A. López-Jiménez, Influence of VOF technique, turbulence model and discretization scheme on the numerical simulation of the non-aerated, skimming flow in stepped spillways, *J. Hydro-environ. Res.* 19 (2018) 137–149, doi:[10.1016/j.jher.2017.10.002](#).
- [25] P. Lopes, J. Leandro, R.F. Carvalho, Self-aeration modelling using a sub-grid volume-of-fluid model, *International Journal of Nonlinear Sciences and Numerical Simulation* 18 (7–8) (2017), doi:[10.1515/ijnsns-2017-0015](#).
- [26] C. Hirt, B. Nichols, Volume of fluid (VOF) method for the dynamics of free boundaries, *J. Comput Phys* 39 (1) (1981) 201–225, doi:[10.1016/0021-9991\(81\)90145-5](#).
- [27] S.B. Pope, *Turbulent flows*, Cambridge University Press, 2000.
- [28] J. Brackbill, D. Kothe, C. Zemach, A continuum method for modeling surface tension, *J. Comput Phys* 100 (2) (1992) 335–354, doi:[10.1016/0021-9991\(92\)90240-Y](#).
- [29] H. Rusche, *Computational fluid dynamics of dispersed two-phase flows at high phase fractions*, Imperial College of Science, Technology and Medicine, 2002 Ph.D. thesis.
- [30] F. Menter, Zonal two equation $k-\omega$ turbulence models for aerodynamic flows, in: *23rd Fluid Dynamics, Plasmadynamics, and Lasers Conference*, American Institute of Aeronautics and Astronautics, 1993, doi:[10.2514/6.1993-2906](#).
- [31] N. Viti, D. Valero, C. Galtieri, Numerical simulation of hydraulic jumps. part 2: recent results and future outlook, *Water (Basel)* 11 (1) (2018) 1–18, doi:[10.3390/w11010028](#).
- [32] Z. Qian, X. Hu, W. Huai, A. Amador, Numerical simulation and analysis of water flow over stepped spillways, *Sci. China Ser. E: Technol. Sci.* 52 (7) (2009) 1958–1965, doi:[10.1007/s11431-009-0127-z](#).
- [33] T. Shih, W.W. Liou, A. Shabbir, Z. Yang, J. Zhu, A new $k-\epsilon$ eddy viscosity model for high reynolds number turbulent flows, *Computers & Fluids* 24 (3) (1995) 227–238, doi:[10.1016/0045-7930\(94\)00032-t](#).
- [34] W. Fan, H. Anglart, Varrhoturbvof: a new set of volume of fluid solvers for turbulent isothermal multiphase flows in openfoam, *Comput Phys Commun* 247 (2020) 106876, doi:[10.1016/j.cpc.2019.106876](#).
- [35] R.I. Issa, Solution of the implicitly discretised fluid flow equations by operator-splitting, *J. Comput Phys* 62 (1) (1986) 40–65.

- [36] P.K. Sweby, High resolution schemes using flux limiters for hyperbolic conservation laws, *SIAM J Numer Anal* 21 (5) (1984) 995–1011, doi:[10.1137/0721062](https://doi.org/10.1137/0721062).
- [37] S.T. Zalesak, Fully multidimensional flux-corrected transport algorithms for fluids, *J Comput Phys* 31 (3) (1979) 335–362, doi:[10.1016/0021-9991\(79\)90051-2](https://doi.org/10.1016/0021-9991(79)90051-2).
- [38] S.M. Damián, *An extended mixture model for the simultaneous treatment of short and long scale interfaces*, National University of the Littoral, 2013 Ph.D. thesis.
- [39] H. Chanson, Stepped spillway flows and air entrainment, *Can. J. Civ. Eng.* 20 (3) (1993) 422–435, doi:[10.1139/l93-057](https://doi.org/10.1139/l93-057).
- [40] R. Clift, J. Grace, M. Weber, M. Weber, *Bubbles, drops, and particles*, Academic Press, 1978.
- [41] M. Brocchini, D.H. Peregrine, The dynamics of strong turbulence at free surfaces. part 1. description, *J Fluid Mech* 449 (2001) 225–254, doi:[10.1017/S0022112001006012](https://doi.org/10.1017/S0022112001006012).
- [42] G. Rotte, M. Kerkvliet, T. van Terwisga, Exploring the limits of RANS-Vof modelling for air cavity flows, *Int. Shipbuild. Prog.* 66 (4) (2020) 273–293, doi:[10.3233/isp-190270](https://doi.org/10.3233/isp-190270).